Materials Today Communications 54 (2026) 115546

Contents lists available at ScienceDirect

Materials Today Communications

journal homepage: www.elsevier.com/locate/mtcomm

Correlating structure and viscoelastic behavior of 3D-printed PLA/PHA blends: Experimental and simulation

Kardo Khalid Abdullah [a], Szabolcs Krizsma [a], Péter Széplaki [a], Kolos Molnár [a,b,c,*]

[a] *Department of Polymer Engineering, Faculty of Mechanical Engineering, Budapest University of Technology and Economics, Műegyetem rkp. 3., Budapest H-1111, Hungary*
[b] *HUN-REN-BME Research Group for Composite Science and Technology, Budapest University of Technology and Economics, Műegyetem rkp. 3., Budapest H-1111, Hungary*
[c] *MTA-BME Lendület Sustainable Polymers Research Group, Budapest University of Technology and Economics, Műegyetem rkp. 3., Budapest H-1111, Hungary*

ARTICLE INFO

Keywords:
PLA/PHA blends
3D printing
Surface morphology
Topography
Viscoelastic modeling

ABSTRACT

Polylactic acid (PLA) is widely used in 3D printing, but its brittleness limits its use in shape-memory applications. Polyhydroxyalkanoates (PHA) are more flexible and crystalline, yet their thermal instability complicates processing. To overcome these limitations, we blended PLA with two semi-crystalline PHA grades: PLA/PHAS (70/30 wt%) and PLA/PHI (70/30 wt%) to combine printability with tailored thermal and viscoelastic properties. Filaments were melt-extruded and printed by fused filament fabrication. Oscillatory melt rheology at the printing temperature (220 °C) showed that the blends exhibited higher elasticity than neat PLA. Scanning electron and atomic force microscopy revealed that neat PLA exhibited a smooth, single-phase surface, whereas both blends showed a phase-separated matrix–droplet morphology with spherical PHA domains. Differential scanning calorimetry confirmed immiscibility through two distinct glass transitions (PHA-rich near 3–4 °C, PLA-rich near 54–55 °C). Both blends showed lower cold-crystallization enthalpies than printed PLA, indicating that the PHA phase hinders the mobility of the PLA chains. X-ray diffraction showed that pure PLA formed only mesomorphic domains (< 1 nm), while the blends developed hierarchical crystalline structures containing large lamellae (24–29 nm) alongside smaller crystallites ($\sim$6–7 nm). A Prony-series finite element model, calibrated using time–temperature superposition from creep test data, accurately predicted linear viscoelastic behavior below the glass transition, remaining reliable up to 40 °C for PLA/PHAS and 45 °C for PLA/PHI. These results demonstrate that blending PLA with PHA enables tunable crystalline structures and predictable viscoelasticity, supporting the development of biomaterials with a functional thermal response.

1. Introduction

Biodegradable polymer scaffolds are widely used in tissue engineering due to their biocompatible and ability to support cell adhesion, proliferation, and tissue formation [1,2]. Common materials for these scaffolds include polyester polymers such as poly(lactic acid) (PLA) and bacterial polyhydroxyalkanoates (PHAs), which have been extensively applied in biomedical applications [3–6]. In recent years, responsive polymers with distinct thermomechanical transitions have gained growing interest in scaffold fabrication [7,8]. These materials—often classified as shape-memory polymers (SMPs)— are capable of alerting their structure in response to external stimuli (*e.g.*, heat or light) [9–11]. In the tissue engineering field, such properties are highly valued because they can theoretically allow scaffolds to adapt to irregular defect shapes, minimizing surgical trauma and enabling delivery through minimally invasive procedures [12–14]. However, effectively leveraging these features requires a deep understanding of the underlying transitions, which depend on a polymer architecture featuring stable net points and reversible domains [15,16]. In semicrystalline polymers, crystalline lamellae serve as structural net points, while amorphous chain segments act as the switchable phase [17]. Thus, the arrangement and degree of crystallinity critically influence these underlying thermomechanical transitions and the resulting structural stability of the scaffolds.

PLA is ideal for 3D printing because of its ease of processing and high initial modulus [18]. It is bio-based and can be biocompatible [19–21]. However, neat PLA is relatively brittle, hydrophobic, and degrades

---

* Corresponding author at: Department of Polymer Engineering, Faculty of Mechanical Engineering, Budapest University of Technology and Economics, Műegyetem rkp. 3., Budapest H-1111, Hungary.
E-mail address: molnar.kolos@gpk.bme.hu (K. Molnár).

https://doi.org/10.1016/j.mtcomm.2026.115546
Received 7 May 2026; Received in revised form 9 June 2026; Accepted 12 June 2026

slowly *in vivo* [22–24]. Its glass-transition temperature of around 60 °C also limits body-temperature actuation in SMP applications unless plasticizers or secondary phases are used [25]. Nevertheless, fused filament fabrication (FFF)-printed PLA can be programmed into temporary shapes and reliably recover upon reheating, demonstrating its potential as an SMP [26]. Building on these strategies, near-infrared light actuation and embedded internal strain have been explored [27]. Additionally, blending PLA with other materials can further control SMP behavior. For example, incorporating PHA into PLA alters crystallinity, ductility, and thermal transitions, thereby altering the effectiveness of the switchable phase [28]. However, unoptimized blends with excessive crystallinity or phase heterogeneity can impair mechanical performance and thermal stability [29].

Due to these limitations, PLA is often blended with softer polymers or polymers with lower glass transition temperatures (T_g), such as poly (ethylene glycol) (PEG), poly(ε-caprolactone) (PCL), or PHA [30,31]. PHAs, including poly(3-hydroxybutyrate) (PHB) and its copolymers, offer excellent biodegradability and biocompatibility [32]. However, PHA is difficult to processing due to its high crystallinity and narrow thermal processing window [33]. For instance, PHB has a low elongation at break (4–10%) and a very high degree of crystallinity (≈60–80%), while its melting temperature (~175 °C) close to the onset of its degradation [34]. This narrow thermal processing window complicates melt extrusion and printing. Recent studies further demonstrate that the printability of blends containing PHA is strongly governed by rheological behavior, crystallinity, and filament stiffness. For example, in poly(3-hydroxybutyrate-co−3-hydroxyvalerate) (PHBV)-based systems, low-stiffness, high-viscosity blends tend to buckle during printing. In contrast, compositions with ≥ 20 wt% PHBV results in smoother and more stable filament extrusion, although higher PHBV content can lead to defects such as warpage [35].

As a result, PHA is most often incorporated into PLA matrices, where it alters phase morphology, mechanical properties and the degree of crystallinity, while maintaining biodegradability [4,36]. PLA blended with PHA copolymers at a 70/30 wt% ratio has been reported to have a favorable balance of stiffness, ductility, and degradation behavior across different processing routes [37–39]. Similarly, blends of a high percentage of PLA and other polymers, like polybutylene adipate terephthalate (PBAT), have shown that a PLA/PBAT (70/30) composition provides excellent printability and improves interfacial quality [40]. This performance is due to altered crystallization and well-dispersed PHA phases in the PLA matrix. However, mechanical and shape-memory properties strongly depend on processing and thermal conditions. Precise extrusion and cooling are key to consistent quality, 3D-printing-compatible PLA/PHA filaments.

The morphology of PLA/PHA blends governs their structural organization and phase distribution. These systems typically exhibit a heterogeneous two-phase structure due to limited miscibility between the components [4,41]. In such systems, the PHA phase is commonly observed as spherical or near-spherical domains dispersed within the continuous PLA matrix [41]. These domains can be as small as nanometric sizes, depending on the conditions of the processing method. For instance, PHA particles have been reported mainly in the 50–450 nm range, with an average size of around 275 nm [42]. Beyond conventional imaging, techniques such as atomic force microscopy (AFM) can be used in analyzing the topography and spatial distribution of these phases [43–47]. This phase-separated architecture shapes the spatial distribution of crystalline and amorphous regions, making it a critical consideration when thermal transitions and viscoelastic behavior are interpreted. An additional but often underreported challenge is preparing PLA/PHA filaments for 3D printing. Numerous studies have focused on commercially available filaments rather than on in-house fabrication [29,48–53]. Filament quality relies on melt homogeneity, steady extrusion, and accurate cooling during drawing and calibration. Insufficient cooling leads to stickiness and diameter fluctuations, reducing print quality [54]. Extrusion of PLA/PHA blends is particularly challenging due to PHA's tendency to crystallize and its limited processing window. Effective cooling, melt stabilization, mixing, and thermal control are essential for consistent filaments for printing functional polymer structures.

Finite-element models have been used to establish quantitative correlations between stiffness and shape fixity, but recovery ratios remain largely unexplored [55]. The creep behavior of a material governs its dimensional stability and time-dependent deformation. In semicrystalline polymers such as PLA, creep arises from time-dependent molecular rearrangement within amorphous regions and from constrained mobility imposed by crystalline domains. Several authors have utilized generalized viscoelastic frameworks including Prony-series representations of generalized Maxwell or Kelvin–Voigt models, to characterize the time-dependent mechanical response of thermoplastic polymers [56]. These approaches capture the distribution of relaxation times associated with molecular motions and are widely used in finite element simulations of polymer creep and stress relaxation behavior. Studies of additively manufactured polymers demonstrate that linear viscoelastic models, specifically those utilizing Prony series, can effectively describe creep deformation. These models not only replicate experimental creep strains but also serve as a predictive tool for long-term deformation in printed thermoplastics [57]. Prony-series parameterizations have been shown to fit relaxation and creep data for 3D-printed PLA components, although predictive accuracy often declines near or above T_g due to nonlinear cooperative segmental motion [58,59]. However, the predictive accuracy of these linear models is often limited to temperatures below T_g, where molecular mobility remains restricted and linear viscoelasticity applies. Near or above T_g, cooperative segmental motions lead to nonlinear mechanical behavior, which cannot be fully captured with parameters derived from sub-T_g measurements.

Nonetheless, the quantitative correlations linking this behavior to PHA content, crystallinity, and thermal transitions remain largely unexplored. Specifically, there is a lack of data on how PHA content influences the evolution of crystallinity and the modification of thermal transitions. Understanding these links is especially important for tailoring thermomechanical behavior, as the phase responsible for deformation resistance is linked to the material's thermal transitions and viscoelastic properties [60,61]. In this study, we hypothesize that adding different commercial grades of PHA to PLA at a 70/30 wt% ratio creates a heterogeneous two-phase structure. This phase-separated morphology is likely to affect thermal transitions, crystalline structures, and viscoelastic creep behavior. We also hypothesize that the dispersed PHA phase influences crystallization and chain mobility within the PLA matrix. These effects are explored through a combination of experimental characterization and computational modeling. The resulting materials hold promises for advancing functional thermal-response biomaterials.

2. Materials and methods

2.1. Materials

PLA pellets (Ingeo™ 3D850 grade) were purchased from NatureWorks LLC (Minnetonka, MN, USA). This grade of PLA is designed for FFF 3D printing, with a D-lactide content of about 4% and a melting temperature between 165 and 180 °C.

Semi-crystalline PHA pellets (PHACT S1000P grade) were supplied by CJ Biomaterials (CJ CheilJedang, Seoul, South Korea), with a melting temperature range of 145–175 °C. This type of PHA is abbreviated as PHAS in this study.

Another semi-crystalline PHA (PHI 002 grade) was supplied in pellet form by NaturePlast (Mondeville, France), with a melting temperature range of 165–175 °C. This type of PHA is abbreviated as PHI in this study.

Amorphous PHA pellets (PHACT A1000P grade) were supplied by CJ Biomaterials (CJ CheilJedang, Seoul, South Korea), with a melting temperature range of 135–175 °C. This type of PHA is referred to as amorphous PHA in this study.

Pellet dimensions were measured with a digital caliper (n = 15 per material). The longest and shortest dimensions are summarized in Supplementary Materials (Appendix 1, Table A.1).

2.2. Filament preparation

All polymer pellets were dried overnight (16 h) in a vacuum drying chamber (Binder VD 53, Germany) at 50 °C. This process was performed before filament fabrication to remove residual moisture and reduce the risk of hydrolytic degradation during melt processing. After drying, we carefully weighed the materials to prepare four batches: neat PLA, PLA/PHAS (70/30 wt%), and PLA/PHI (70/30 wt%). Each batch was manually dry-mixed in a barrel by manually shaking for about 120 s until it appeared visually uniform. All pellets had similar minimum dimensions of approximately 3.0–3.5 mm and similar density, reducing the risk of segregation during handling. To prevent segregation after mixing, we transferred the batches directly to the extruder hopper without intermediate storage or vibration. Final homogenization is expected to occur in the twin-screw extruder equipped with kneading elements for both distributive and dispersive mixing.

We initially targeted PLA/amorphous PHA blends with higher amorphous PHA content (70/30 and 80/20 wt% PLA/amorphous PHA blends), but these formulations were not processable during filament extrusion. They exhibited excessive stickiness and irregular flow, preventing the formation of a continuous filament. Only the blend containing 10 wt% amorphous PHA (90/10 wt% PLA/amorphous/PHA) yielded a stable extrudate filament. However, this filament failed when we attempted to print it using the parameters described in Section 2.3 3D printing (Table 2). The filament, even with a small amount of amorphous PHA, exhibited low thermal stability and lacked a distinct melting point, leading to gradual softening and tackiness at the nozzle rather than consistent flow performance. Due to insurmountable issues at both the extrusion and printing stages, we excluded this filament (PLA/amorphous PHA 90/10 wt%) from further consideration in this study.

We therefore fabricated the filaments using a twin-screw extruder with co-rotating screws (LTE 26–44, Labtech Engineering Co., Ltd., Samutprakarn, Thailand) to achieve effective melt mixing and the uniform dispersion of all components. The diameter of the screws was 26 mm with an L/D ratio of 44:1, and rotation speed was set at 20 rpm. A filament die with a 3 mm diameter hole was used. The extrusion parameters are summarized in Table 1.

After extrusion, the melted extrusion filament is passed through two consecutive cooling baths (water), which stabilizes its geometry and minimizes post-extrusion deformation. Surface moisture was removed with a clean, lint-free cloth before winding. Filament diameters were continuously measured with an inline laser measurement system (ODAC 13 TRIO, Zumbach Electronic AG, Orpund, Switzerland). The system targeted a nominal diameter of 1.75 mm with a tolerance of ±0.05 mm, enabling continuous data acquisition and real-time monitoring (MeasureOD software). A representative video recording of the extrusion and diameter measurement setup is provided in the Supplementary Materials (Appendix 1, Video A.1). Three filaments were produced: one from neat PLA and two from the PLA/PHA blends. The filaments were stored overnight and then specimens were 3D printed with them.

2.3. 3D printing

We used FFF technology to print the specimens from fabricated filaments on a 3D printer (P1S, Bambu Lab, China) with a 256 mm × 256 mm × 256 mm build platform. We printed solid rectangular bars (4 mm × 10 mm × 60 mm) from the three successfully produced filaments and used these specimens in further characterization. For X-ray diffraction (XRD) and melt rheology, cylindrical specimens were printed with complete infill. The XRD specimens were 1 mm thick and 22 mm in diameter. For the melt rheology analysis, which consisted of oscillatory frequency-sweep measurements on a rotational rheometer, the specimens were 25 mm in diameter and 0.8 mm thick. Additionally, rectangular specimens measuring 4 mm × 10 mm × 80 mm were fabricated for three-point bending tests. We used a 0.2 mm nozzle and 100% infill to ensure full material density for thermal, structural, and mechanical characterization. Nozzle temperature was set to 220 °C, the build platform was maintained at 65 °C, and a textured polyetherimide plate was used to enhance interlayer adhesion and reduce warping. We selected moderate printing speeds to improve dimensional accuracy and reduce printing artifacts, as shown in Table 2.

In the preliminary printing test, three filaments were printable with these printing conditions, including: i. PLA, ii. PLA/PHAS, and iii. PLA/PHI. To enhance clarity in this study, we abbreviated the samples, as shown in Table 3.

2.4. Characterization

We used various complementary techniques to analyze the materials at different processing stages and establish structure–property relationships. To assess printability, we printed the filaments, and compared the resulting parts to the CAD models through visual inspection and digital microscopy. To analyze the behavior of the melt flow at the printing temperature and just below it, we conducted oscillatory frequency-sweep rheometry at the melting temperatures. We examined the phase morphology of fractured samples by scanning electron microscopy (SEM) to distinguish between neat PLA and the two blends. We further investigated nanoscale surface topography and phase contrast by atomic force microscopy (AFM) in tapping mode, which provided additional insight into phase distribution and heterogeneity. The impact of processing on thermal transitions and crystallinity was evaluated by differential scanning calorimetry (DSC) on printed specimens and original pellets. To characterize the crystalline order of lamellar structure and size, we conducted X-ray diffraction (XRD) on the printed specimens. We performed three-point bending tests to evaluate the flexural properties of the materials. Finally, we studied time-dependent deformation and validated the Prony-series model with the use of creep testing, combined with time–temperature superposition

Table 2
3D printing speeds.

Layer	Speed (mm/s)
Initial layer	35
Initial layer infill	50
Outer wall	200
Inner wall	300
Internal solid infill	250
Top surface	200

Table 1
Extruder temperature profile (°C) across ten heating zones and the die for PLA and PLA/PHA blends. The PLA/PHA profile was applied to all three PLA/PHA blends (PLA/PHA S1000, PLA/PHI 002, and PLA/amorphous PHA).

Extruder temperature profile (°C)	1	2	3	4	5	6	7	8	9	10	Die
PLA	170	175	180	180	180	185	190	190	195	195	195
PLA/PHA blends	170	170	170	175	175	180	185	185	190	190	190

Table 3
Description of sample identifiers (codes) for 3D-printed specimens.

Description of materials content	Code
PLA 3D850	PLA
PLA 3D850 / PHACT S1000P (70/30 wt%)	PLA/PHAS
PLA 3D850 / PHI 002 (70/30 wt%)	PLA/PHI

(CreepTTS) and viscoelastic finite-element modeling under sub–T_g conditions.

2.4.1. *Printability inspections*

We inspected the printed specimens with a high-resolution digital microscope (VHX−5000 series, Keyence Corporation, Osaka, Japan). The system, equipped with a VH-Z100UT long-range zoom lens (100x to 1000x magnification) and differential interference contrast (DIC) capabilities, enables detailed visualization across a range of scales without the need for a conductive coating.

2.4.2. *Oscillatory frequency sweep measurements*

The melt rheological properties of neat PLA, PLA/PHAS, and PLA/PHI were examined with a rotational rheometer (Kinexus Prime Pro+, Netzsch-Gerätebau GmbH, Selb, Germany). A 25 mm diameter parallel-plate setup was employed, with a measurement gap of 0.8 mm. The printed cylindrical specimen was positioned between the plates and heated to the desired temperature. Oscillatory frequency-sweep measurements were conducted in strain-controlled mode, with a constant shear strain of 1%. Angular frequency ranged from 100 Hz down to 0.1 Hz, with 7 measurement points per decade. Each specimen was measured at three temperatures: 220 °C (the actual 3D printing temperature), 210 °C, and 200 °C. We selected the additional temperatures to evaluate the wider processability window. During each measurement, we recorded the storage modulus (G') and loss modulus (G'') as a function of frequency (f). We calculated the loss tangent (tan δ) as the ratio of G'' to G'. The complex viscosity (η^*) was then calculated from these moduli with Eq. (1).

$$\eta^* = \frac{\sqrt{(G')^2 + (G'')^2}}{2\pi f} \tag{1}$$

2.4.3. *Scanning electron microscopy (SEM)*

We used SEM (JEOL 6380 LA, Tokyo, Japan) to examine the phase morphology of neat PLA and the two blends. The samples were immersed in liquid nitrogen and fractured manually when sufficiently embrittled, which produced clean, brittle surfaces. The fractured specimens were mounted on aluminum stubs with the use of conductive carbon tape and coated with a thin layer of gold with a sputter coater (JEOL JFC−1200, Tokyo, Japan) for 30 s under an argon atmosphere. Images were captured at an accelerating voltage of 5 kV and a magnification of 5000 × . We selected representative areas from each sample to ensure accurate evaluation of phase distribution. To quantify morphological differences, we performed image analysis of the SEM micrographs using ImageJ (version 1.54 g, National Institutes of Health, Bethesda, MD, USA). For each material, ten individual domains were measured.

2.4.4. *Atomic force microscopy (AFM)*

The surface topography and phase contrast of the samples were examined by AFM (FlexAFM 5, Nanosurf, Liestal, Switzerland) in tapping mode (amplitude modulation) with phase imaging. The printed samples were first fractured in liquid nitrogen for fresh cross-sections. The fractured pieces were then embedded in epoxy, clamped vertically, and left to cure. After curing, we polished the embedded samples to obtain a smooth surface for AFM analysis. The measurements were performed with a TAP190AI-G cantilever in air, and both topography (amplitude) and phase-contrast images were recorded in the forward scan direction. AFM images were acquired over an area of 1 µm × 1 µm, with a line time of 1.2 s, a scan rotation of 0°, a setpoint of 60%, and a free vibration amplitude of 1 V.

2.4.5. *Differential scanning calorimetry (DSC)*

We used a differential scanning calorimeter (DSC 300 Caliris Select, Netzsch GmbH, Selb, Germany) to evaluate the thermal properties of the specimens. The specimens included 3D-printed samples (PLA, PLA/PHAS, and PLA/PHI), and PLA, PHAS, and PHI pellets as references. Each sample was cut into small pieces (approximately 1–2 mm). They weighed between 5 and 9 mg and were placed in a sealed aluminum pan, and tested under a nitrogen purge of 20 mL/min. The samples underwent a heat–cool–heat cycle between −50 and 200 °C with a heating/cooling rate of 10 °C/min. Notably, cold crystallization occurred during heating, which was accounted for in the calculations. Peaks were identified with the NETZSCH Assistant software (version 9.7). The first heating cycles showed the T_g of each sample. We calculated the degree of crystallinity (X_c) for a single material using Eq. (2).

$$X_c = \frac{\Delta H_m - \Delta H_{cc}}{\Delta H_{tc}} \times 100 \tag{2}$$

where ΔH_m is the melting enthalpy, ΔH_{cc} is the cold crystallization enthalpy, and ΔH_{tc} is the crystallization enthalpy of the ideally crystalline PLA, which is taken to be 93 J g^{-1} [62], and for PHAS and PHI pellets, which are taken to be 146 J g^{-1} [63].

2.4.6. *X-ray diffraction (XRD)*

XRD patterns were performed on a Bruker D6 Phaser (Bruker AXS SE, Germany) diffractometer with Cu Kα radiation (λ = 1.5418 Å) in Bragg–Brentano geometry. Cylindrical specimens (1 mm thickness, 22 mm diameter) were printed from PLA, PLA/PHAS, and PLA/PHI filaments. Diffraction patterns were recorded over a 2θ range of 6–35° in step-scan mode. Data were collected with a counting time of 0.2 s per step. During acquisition, samples were rotated at 8 rpm, which minimized preferred-orientation effects. Diffraction peaks were obtained, denoised, and then analyzed with the OriginPro software (version 8.6). We evaluated the crystalline order of the lamellar structure, and determined lamellar size from peak broadening using the Scherrer equation [64], as represented in Eq. (3).

$$D = \frac{K\lambda}{\beta \cos\theta} \tag{3}$$

where (D) is crystallite size, (K) is a dimensionless shape factor, (λ) is the X-ray wavelength, (β) is the full width at half maximum in radians, and (θ) is the Bragg angle. Additionally, the degrees of crystallinity of the PLA/PHAS and the PLA/PHI blends were quantified with the OriginPro software (version 8.6). We resolved the crystalline peak areas by applying a multi-point ($n = 10$) baseline fitting to ensure accurate peak integration. The total amorphous area was subsequently integrated directly over the full 2θ range (6° to 35°). The degree of crystallinity was determined with Eq. (4).

$$X_c = \frac{A_c}{A_c + A_a} \times 100 \tag{4}$$

where A_c is the crystalline area, and A_a is the amorphous area.

2.4.7. *Three-point bending*

Flexural properties of the specimens were assessed through a three-point bending test on 3D printed 80 mm × 10 mm × 4 mm bulk block specimens. This test was conducted 5 times per specimen type on a Zwick Z005 universal testing machine (Zwick Roell, Ulm, Germany) equipped with a 5 kN load cell. The support span was fixed at 64 mm, and a 1 N preload was applied before testing. The test started at a crosshead displacement speed of 1 mm/min to precisely measure the flexural modulus, then increased to 5 mm/min for the rest of the test.

Environmental conditions were kept at room temperature and 35–40% relative humidity.

The standard assumes that the specimen can be considered a straight beam throughout the test and limits the strain to 3.5% (approx. 6 mm deflection for the given test specimens). The strains were higher than that, and we wanted to evaluate the entire deformation range. Therefore, we applied nonlinear geometric corrections in accordance with ASTM D790 [65] throughout the evaluation. The flexural stress (σ_f), flexural strain (ε_f), and flexural modulus (E_f) were calculated with Eqs. (5)–(7), respectively. Flexural toughness (U) is determined by the total area under the load-deflection curve up to failure, as presented in Eq. (8).

$$\sigma_f = \frac{3FL}{2bd^2} \quad [1 + 6\left(\frac{D}{L}\right)^2 - \quad 4\left(\frac{d}{L}\right)\left(\frac{D}{L}\right)] \tag{5}$$

$$\varepsilon_f = \frac{6Dd}{L^2} \quad [1 - \left(\frac{D}{L}\right)^2 + \quad 4\left(\frac{d}{L}\right)\left(\frac{D}{L}\right)] \tag{6}$$

$$E_f = \frac{L^3\, m}{4bd^3} \tag{7}$$

$$U = \int \sigma_f \, d\varepsilon_f \tag{8}$$

where (F) is the applied load, (L) is the support span (L=64 mm), (b) is the measured width of the specimen, (d) is the measured thickness of the specimen, (D) is the center deflection, and (m) is the slope of the initial linear portion of the load-deflection curve.

2.4.8. Creep TTS testing

In semicrystalline polymers, maintaining dimensional stability depends on the material's resistance to creep, which is the gradual deformation that occurs under constant stress over time. Understanding how PLA/PHA blends behave under sustained load across a range of temperatures is therefore essential for predicting their time-dependent deformation. Therefore, PLA/PHAS and PLA/PHI blends were subjected to creep testing in an air atmosphere, with a dynamic mechanical analyzer (DMA Q800, TA Instruments, New Castle, DE, United States). The creep tests were performed in creep time-temperature superposition (TTS) mode of the DMA, in a three-point bending arrangement with a standard span of 50 mm. The analyzed specimens had dimensions of 4 mm × 10 mm × 60 mm. Table 4 shows further test parameters.

Creep modulus data were obtained from the tests as the ratios of the pre-set flexural stress to the time-dependent flexural strain. The creep modulus, as defined by Eq. (9), characterizes the material's resistance to creep.

$$E(t) = \quad \frac{\sigma_0}{\epsilon(t)} \tag{9}$$

2.4.9. Finite element formulation

The creep modulus can be approximated with the Prony-series method, which is the sum of the products of individual relative moduli and their corresponding relaxation times. The Prony-series approximation can be written according to Eq. (10).

Table 4
Parameters of DMA creep TTS testing.

Parameters used	Unit	Value
Flexural stress	MPa	2
Minimum temperature	°C	25
Maximum temperature	°C	50
Temperature increment	°C	5
Furnace (conditioning) time	min	10
Creep time	min	30
Recovery time	min	30

$$E(t) = E_\infty + \sum_{i=1}^{N_E} E_i \bullet e^{-t/\tau_i{}^E} \tag{10}$$

where:

E_∞ is the elastic modulus of the completely relaxed material (at t = ∞),
E_i is the i$^{\text{th}}$ elastic component of the Prony-series,
$\tau_i{}^E$ is the relaxation time of the i$^{\text{th}}$ component of the Prony series, and
N_E is the number of Prony terms.

A four-term Prony series was selected as an optimal balance between numerical stability during curve fitting and simulation accuracy. Finite element simulations were conducted in ANSYS Workbench with the use of the generalized Maxwell model. The general stress-strain relationship of this model is described by Eq. (11).

$$\overset{=}{\sigma} \;= \int_0^t 2G(t-\tau) \bullet \frac{\partial \overset{=}{\varepsilon}_d}{\partial \tau} d\tau + \overset{=}{I} \;\bullet \int_0^t K(t-\tau) \bullet \frac{\partial \varepsilon_v}{\partial \tau} d\tau \tag{11}$$

where:

$\overset{=}{\sigma}$ is the Cauchy stress tensor,
$\overset{=}{\varepsilon}_d$is the deviatoric part of the strain tensor,
$\varepsilon_v$is volumetric (hydrostatic) strain,
$\overset{=}{I}$ is the unit tensor,
$G(t)$is the shear relaxation kernel function,
$K(t)$is the bulk relaxation kernel function,
$t$is current time, and
τpast time.

Initial shear and bulk moduli were derived from elastic properties with Eqs. (12) and (13).

$$G(t=0) = G_0 = \frac{E}{2 \bullet (1+\nu)} \tag{12}$$

$$K(t=0) = K_0 = \frac{E}{3 \bullet (1-2\nu)} \tag{13}$$

where ν is the Poisson's ratio of the material.

3. Results and discussion

3.1. Print quality and dimensional accuracy

We first assess the quality of the printed specimens through visual inspection and digital microscopy, as shown in Fig. 1. All specimen types exhibit clean, well-defined features with no visible defects, and the printed geometries closely match the intended CAD design, demonstrating good dimensional accuracy and structural consistency.

These findings confirm that the printing parameters are consistent and reliable across all tested materials. Incorporating blended filaments containing semi-crystalline PHA in PLA (PLA/PHAS and PLA/PHI) does not negatively affect printability or the final quality of the parts under the tested conditions. Having verified the macroscopic integrity of the printed items, we now proceed to thermal analysis to explore how the blends affect the internal microstructure.

3.2. Melt rheology analysis

The oscillatory rheology results show that for all materials, G' and G'' increase as the frequency increases, while the overall loss tangent decreases, as shown in Fig. 2. This behavior reflects typical viscoelastic

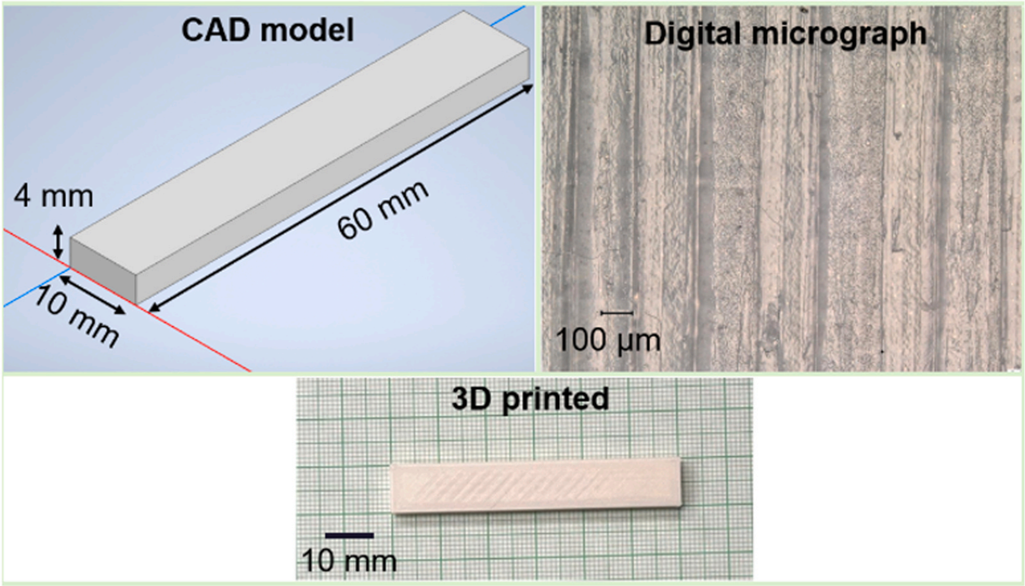

Fig. 1. Visual and digital microscopic inspection of the printed sample and its CAD model.

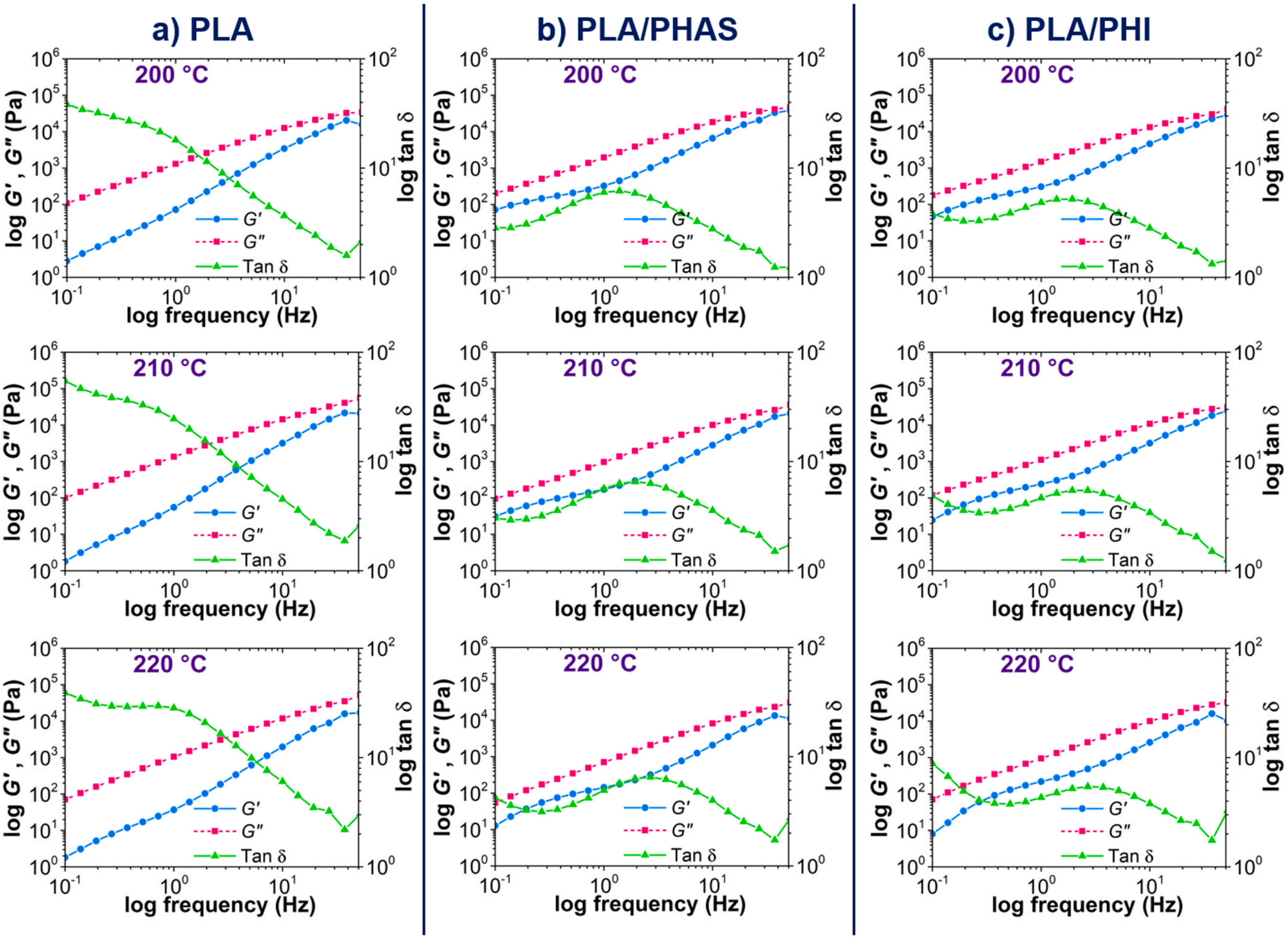

Fig. 2. Rheological melting properties of (a) PLA, (b) PLA/PHAS, and (c) PLA/PHI measured at various temperatures and frequencies.

melt dynamics: polymer chains relax on long timescales (low frequency), leading to a viscous-dominated response, and become increasingly constrained at short timescales (high frequency), resulting in a higher elastic contribution [66,67]. Nevertheless, G'' remains higher than G' over most of the frequency range for all materials. While measurements were taken up to 100 Hz, we cut off the data at 50 Hz during analysis to improve accuracy and remove potential high-frequency inertial artifacts.

The influence of the dispersed PHA phase on melt rheology is most clearly seen at the printing temperature (220 °C). Neat PLA behaves as a primarily viscous melt. Across all frequencies (0.1–50 Hz), its storage modulus is lower than its loss modulus. Its loss tangent remains above 2, exceeding 50 at low frequencies. This shows that neat PLA stores minimal elastic energy under shear. PLA/PHAS exhibits more pronounced elastic behavior than PLA at 220 °C. It has a higher storage modulus across all frequencies, especially below 1 Hz, where its loss tangent is several times lower than for neat PLA. The loss modulus increases, too, but the ratio of loss to storage modulus decreases notably. The maximum loss tangent remains below 7 across all frequencies. This can be attributed to dispersed PHAS domains acting as physical crosslinks that trap elastic energy, especially at low shear rates when the polymer chains have time to interact with the dispersed phase. On the other hand, PLA/PHI shows intermediate elasticity: its storage modulus at low frequencies is clearly above that of neat PLA but remains lower than that of PLA/PHAS below 0.2 Hz. However, as frequency increases, the storage modulus of PLA/PHI surpasses that of PLA/PHAS at frequencies above ~1 Hz. The maximum loss tangent stays below 9 at 0.1 Hz and decreases as the frequency increases.

At 210 °C and 200 °C, each material exhibits distinct rheological melting behavior. Neat PLA shows only minor changes. Its storage and loss moduli increase slightly, and its loss tangent decreases moderately. Hence, it remains mostly viscous-dominated (loss tangent $>$ 1) even at 200 °C. This reflects the absence of any dispersed phase that could form a temperature-sensitive network. On the other hand, PLA/PHAS shows a much stronger temperature response compared to PLA. As the temperature drops to 210 °C and then to 200 °C, its loss modulus rises significantly, and its storage modulus increases by more than an order of magnitude compared to values at 220 °C. Concurrently, its loss tangent decreases with temperature. PLA/PHI behaves similarly at lower temperatures, but the temperature sensitivity of PLA/PHAS is stronger, which is consistent with its finer phase dispersion.

Beyond the storage and loss moduli, the complex viscosity provides additional insight into flow behavior, as shown in Fig. 3. All materials exhibit strong shear-thinning behavior, with complex viscosity decreasing with increasing frequency. At 220 °C (printing temperature), PLA/PHAS exhibits a distinctive non-monotonic pattern: its complex viscosity slightly increases from 0.1 Hz to about 10 Hz, then declines beyond that point. Despite this, PLA/PHAS maintains the lowest complex viscosity among all materials. Lower viscosity means easier flow and reduced extrusion forces. On the other hand, neat PLA has an intermediate complex viscosity. The complex viscosity of PLA/PHI is marginally higher than that of neat PLA below approximately 0.6 Hz, but above 1 Hz, it is lower.

Temperature sensitivity varies significantly among the three materials. When the temperature decreases from 220 °C to 200 °C, PLA/PHAS shows the largest change, with its low-frequency complex viscosity increasing by more than 3-fold, indicating a gel-like transition. PLA/PHI shows a smaller, more stable shift, maintaining consistent flow over a wider temperature range. In contrast, neat PLA exhibits irregular, non-monotonic temperature dependence: at 210 °C, its complex viscosity exceeds that at 200 °C for certain frequencies. This may be due to residual crystallites or thermo-oxidative effects. Beyond ~30 Hz, PLA at 200 °C has even lower viscosity than at 220 °C.

From a processing standpoint, PLA/PHAS flows well at 220 °C but is very sensitive to temperature changes. Printing below 210 °C can be challenging. In comparison, PLA/PHI has a more consistent complex viscosity across different temperatures. Neat PLA's unpredictable temperature response may lead to uneven extrusion when the temperature

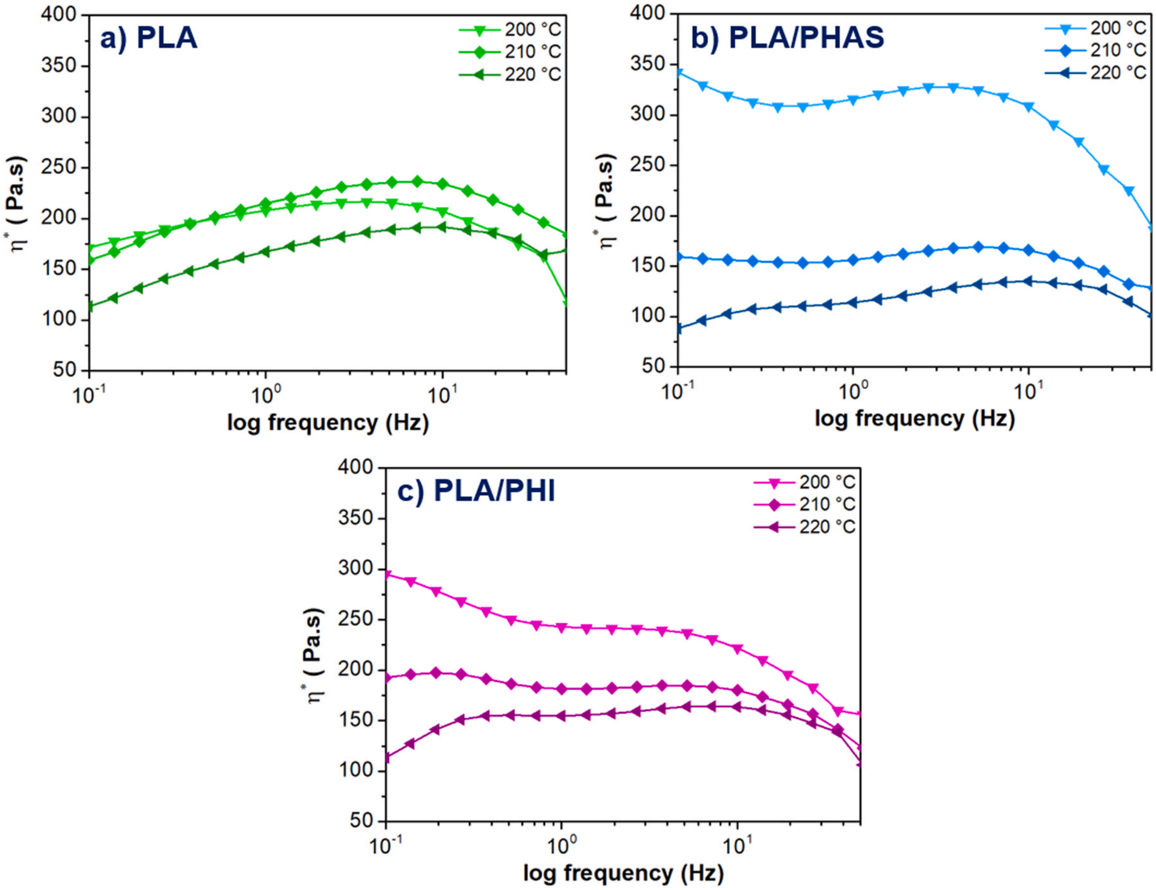

Fig. 3. Complex viscosity (η*) as a function of frequency for neat PLA, PLA/PHAS, and PLA/PHI at 200 °C, 210 °C, and 220 °C.

varies.

Optimal printing temperatures are identified from rheological data. This equilibrium between viscous flow and elastic recovery is considered essential for effective extrusion processing of thermoplastic polymers [68,69]. Based on the literature [70,71], we considered that the shear rate inside the nozzle during extrusion corresponds to oscillatory frequencies in the range of 10–40 Hz. At 220 °C, a low storage modulus and a high loss tangent enhance mobility, facilitate better flow, and lead to smoother extrusion of the blends. In the shear rate range of 10–40 Hz—relevant to nozzle flow—PLA/PHAS shows the most characteristic behavior: it has the highest complex viscosity at 200 °C but the lowest at 220 °C. Neat PLA and PLA/PHI have nearly identical complex viscosities at 200 °C, but the differences become evident as the temperature increases. At both 210 °C and 220 °C, PLA/PHI exhibits a lower viscosity than neat PLA. This suggests that adding PHI or PHAS reduces flow resistance at higher temperatures, with PLA/PHAS providing the greatest improvement in processability at 220 °C.

3.3. *Phase morphology analysis*

The SEM images of fractured surfaces reveal clear morphological differences between neat PLA and the two blends (Fig. 4). Neat PLA exhibits a smooth, relatively homogeneous surface, consistent with a single continuous phase. In contrast, both PLA/PHAS and PLA/PHI exhibit heterogeneous, phase-separated morphology, with the continuous PLA matrix interrupted by dispersed PHA-rich domains. These features correspond to a second polymer phase rather than voids. Limited miscibility in these blends typically results in a matrix–droplet morphology. The dispersed PHA phase appears as nanometric spherical or near-spherical particles. This observation is consistent with the literature [4,41,42].

Neat PLA showed no discrete domains; occasional surface features (4.25 ± 2.44 μm) can be attributed to fracture surface roughness rather than a dispersed phase. The two blends are not morphologically identical. PLA/PHAS appears to contain a finer, more uniformly distributed dispersed phase, within an average domain diameter of 0.65 ± 0.19 μm, and a relatively narrow size distribution. PLA/PHI shows less regular domains, indicating that phase dispersion varies with blend composition, with an average domain diameter of 1.53 ± 0.73 μm. From a functional perspective, this phase-separated structure is important because it controls the spatial distribution of crystalline and amorphous regions, thereby influencing thermal and viscoelastic properties. These quantitative results confirm the qualitative observation that PLA/PHAS has a finer, more uniformly distributed dispersed phase than PLA/PHI. The individual domain measurements for each sample are provided in the Supplementary Materials (Appendix 1, Tables A.2.–A.4). To complement the phase morphologies of the samples, we further analyze surface topography and phase contrast in the next section, offering deeper insight into phase distributions and heterogeneity.

3.4. *Surface topography and phase contrast*

The AFM surface topography images reveal distinct morphological features depending on the composition of the samples (Fig. 5). Neat PLA exhibits a smooth, uniform surface and a consistent phase signal, indicating a single-phase structure. In contrast, both blends display rougher surfaces with distinct topographical domains, indicating the presence of a dispersed second phase within the PLA matrix. These topographical features reveal the nanoscale structure of the blends and confirm that phase separation occurs after blending.

Phase-contrast imaging provides additional insight into local variations in material response. Neat PLA shows a relatively uniform phase signal. Both blends, however, exhibit clear phase contrast, confirming the presence of regions with different material properties. Additionally, PLA/PHAS exhibits a finely distributed contrast pattern, indicating a regular, well-dispersed phase morphology. The phase contrast of PLA/PHI is more pronounced compared to PLA/PHAS. These observations align with SEM findings and confirm that the phase morphology depends on the specific PHA derivative used. Overall, the AFM results support the formation of a two-phase structure in the blends. This hierarchical morphology is important because it reflects the internal organization of the blends and helps explain the thermal and viscoelastic

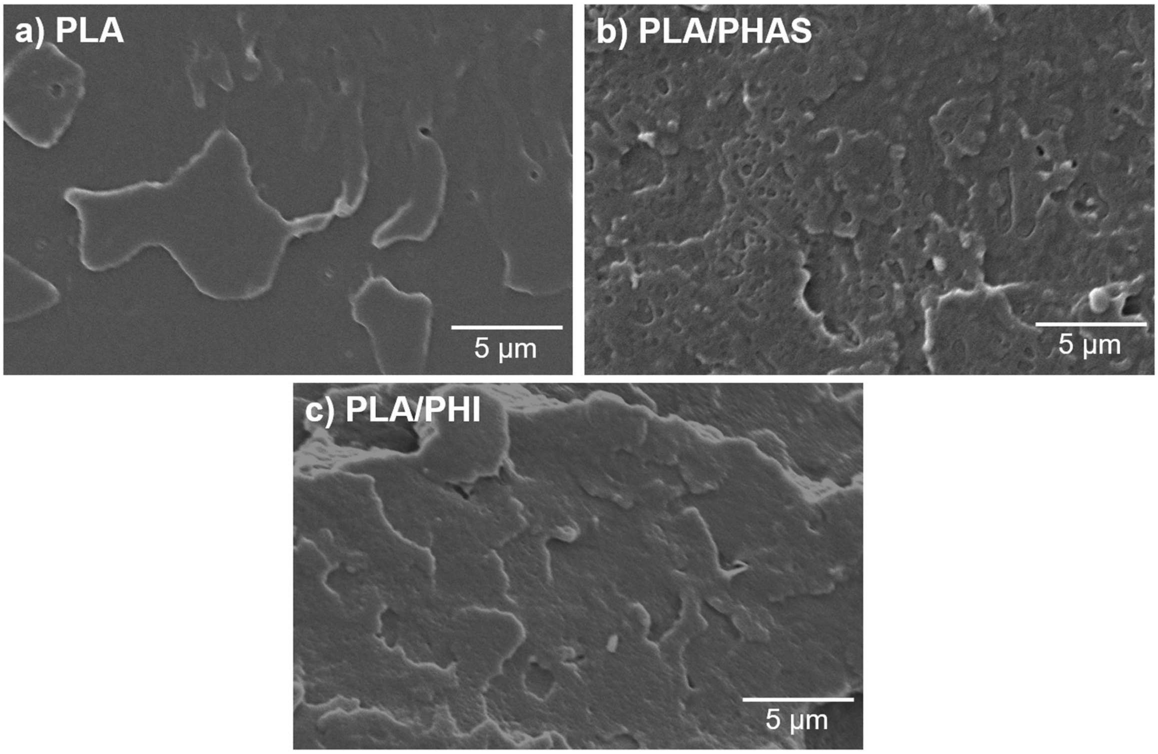

Fig. 4. SEM images of fracture surface morphology.

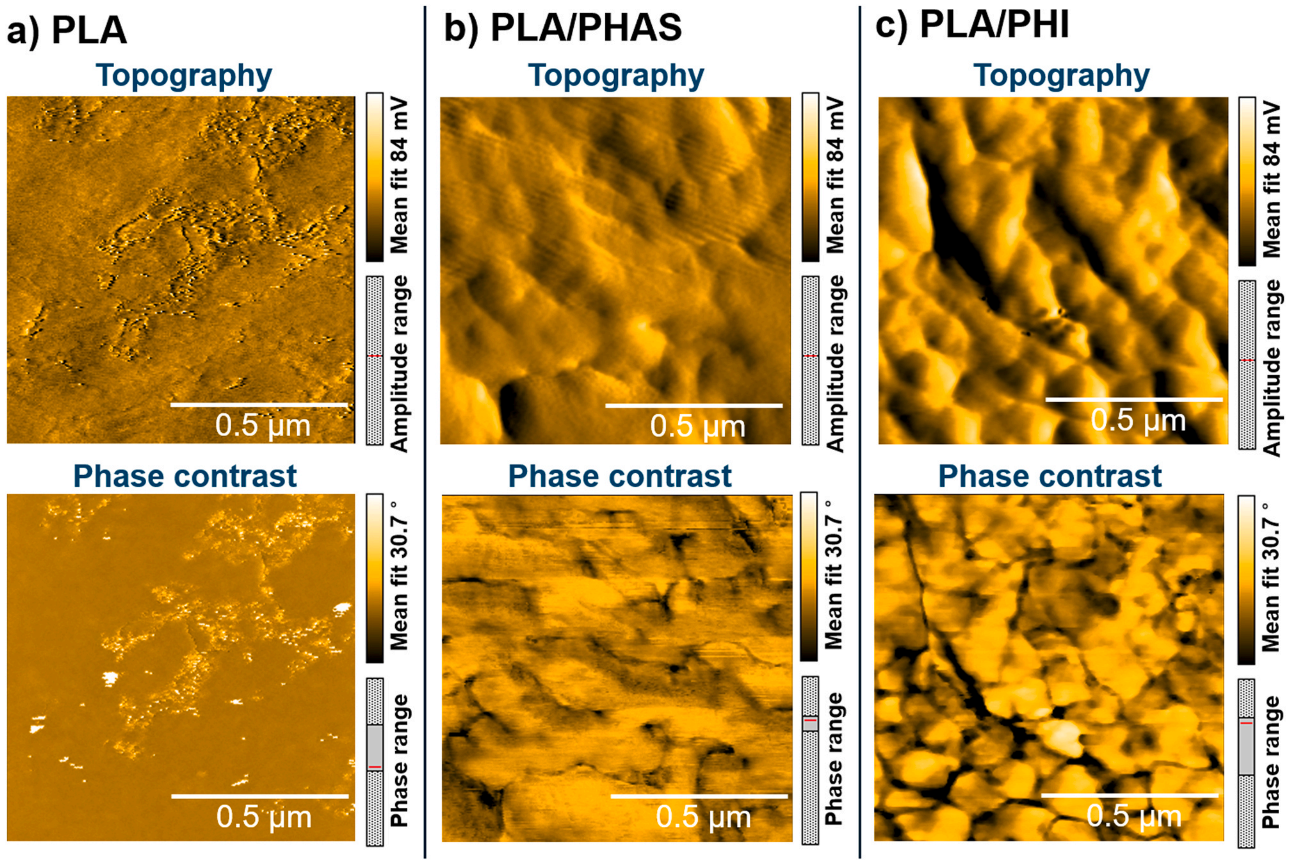

Fig. 5. Surface topography and phase-contrast images obtained by AFM.

behavior discussed in the following sections.

3.5. *Thermal properties analysis*

We analyze the thermal properties of the materials based on their initial heating DSC curves. Fig. 6 shows the thermograms obtained during the first heating cycle, allowing the identification of glass transition, cold-crystallization (exotherm), and melting (endotherm) enthalpies.

Neat PLA pellets show a single glass transition at 55.7 °C, while printed PLA has a T_g of 55.5 °C, indicating that the printing process does not significantly alter the T_g of pure PLA. However, the degree of crystallinity decreases from 29% (pellets) to 27% (printed). This slight reduction suggests that the printing process partially disrupts the ordered structure of PLA, likely due to rapid cooling during deposition, thereby reducing the time available for crystal growth. In contrast, PHA and PHI pellets exhibit higher degrees of crystallinity than PLA pellets. These differences in crystallinity could also affect the phase behavior and interfacial properties of the blended polymers. However, the current DSC data cannot determine the degree of crystallinity in the blends because the melting peaks of the components overlapped. The thermal properties obtained from the first heating cycle are presented in Table 5.

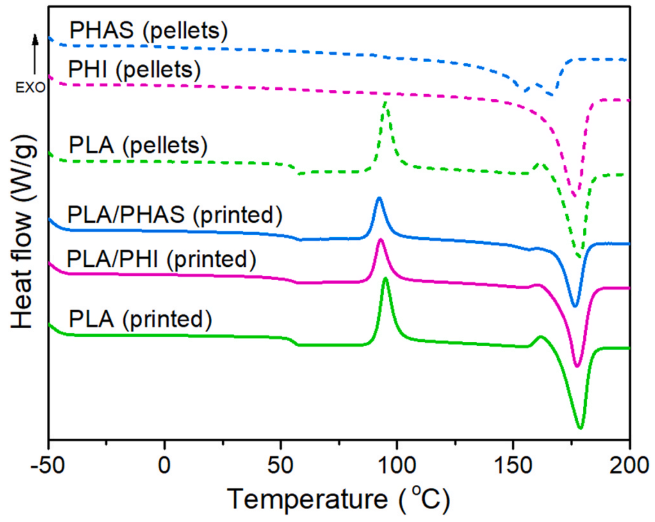

Fig. 6. DSC curves obtained from the first heating cycle.

The printed PLA/PHAS and PLA/PHI blends each exhibit two distinct glass transitions, which correspond to the separate T_g values of the PLA and PHA phases. This observation confirms that both blends are immiscible and phase-separated, directly supporting the AFM findings. Regarding crystallization, both blends exhibit lower cold-crystallization enthalpies than printed PLA, indicating that the PHA phase hinders PLA

Table 5
Thermal properties obtained from the first heat cycle from DSC scans.

Samples	First T_g (°C)	Second T_g (°C)	ΔH_m (J g^{-1})	ΔH_{cc} (J g^{-1})	Degree of crystallinity (%)
PLA pellets	55.7	-	57.3	30.4	29
PHAS pellets	–3.2	-	49.5	-	34
PHI pellets	–2.8	-	77.6	-	53
PLA printed	55.5	-	55.7	30.5	27
PLA/PHAS printed	3.9	54.2	43.3	18.7	-
PLA/PHI printed	3.0	55.0	53.2	20.7	-

chain mobility. Overall, the thermal analysis confirms the immiscible two-phase structure in the blends. In the next section, we focus on the crystalline structures and lamellar sizes.

3.6. XRD peak analysis

XRD peaks reveal primarily distinct crystalline characteristics for neat PLA and the two PHA blends. Neat PLA exhibits a single broad halo at 2θ = 16.53° with a large FWHM (10.44°), indicating very poor long-range order. Scherrer analysis gives an apparent crystallite size of ~0.8 nm, consistent with rudimentary or mesomorphic domains (Fig. 7). The presence of a broad diffraction halo combined with very small crystallites suggests that the structure is predominantly mesomorphic rather than fully crystalline. This mesomorphic ordering usually occurs during rapid cooling or thermo-mechanical processing. In such situations, polymer chains can partially align but do not have enough time to form stable lamellar crystals. Similar behavior has been observed for PLA processed under comparable thermal conditions [25, 72].

In contrast, the PLA/PHI and PLA/PHAS blends exhibit multiple well-defined Bragg reflections. These peaks indicate a more organized crystalline structure than that of neat PLA. The baseline-corrected diffraction patterns and peak-fitting results are provided in Fig. A.1 in the Supplementary Materials (Appendix 1).

The two blends show hierarchical distributions of crystallite sizes, including small (~0.7–2 nm), intermediate (~3–8 nm), and large (~24–29 nm) crystallites. For PLA/PHI, crystallite sizes range from approximately 1.4–29.2 nm, with an average of about 7.0 nm (Table 6). PLA/PHAS crystallite sizes range from ~0.8–24.3 nm, with an average of ~6.3 nm (Table 7). The narrow, intense reflections correspond to well-ordered crystalline lamellae, likely originating from PLA α-form crystals or PHA crystalline domains. In contrast, broader reflections correspond to smaller or less perfect crystallites.

Peak deconvolution combined with the Scherrer equation allows estimation of the crystalline fraction detected by XRD. The degree of crystallinity is calculated as 19.3% for PLA/PHI and 16.0% for PLA/PHAS. These values indicate the proportion of well-ordered crystalline regions within the blends. However, XRD measures only the crystalline fraction, excluding imperfect crystals and total crystallinity.

From a structural perspective, these crystalline regions contribute to the hierarchical crystalline architecture of semicrystalline polymer blends. In established semicrystalline SMPs, well-defined lamellar crystals act as fixed net points that maintain the permanent shape, while smaller crystallites and amorphous regions facilitate reversible deformation [73–75]. The hierarchical crystallinity observed in our PLA/PHA blends—particularly the coexistence of large (≈24–29 nm) and small (≈1–7 nm) crystallites—suggests a structural architecture that could, in principle, support shape-memory mechanisms. Overall, XRD results reveal clear structural differences between the blends and neat PLA. To assess whether these differences influence the mechanical properties, we subsequently performed three-point bending tests, as described in the following section.

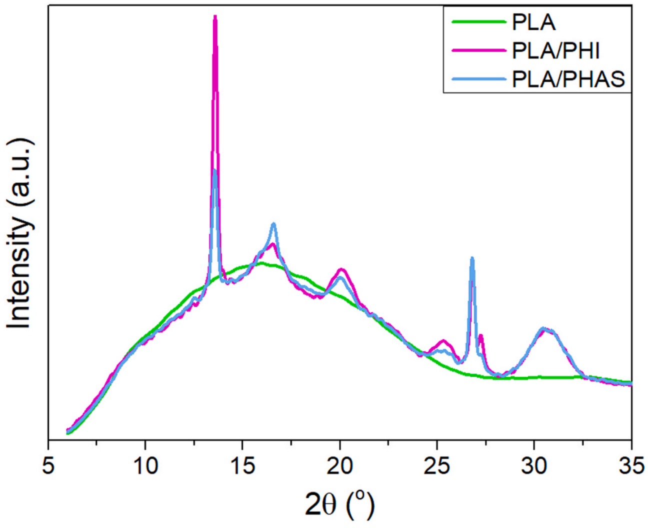

Fig. 7. X-ray diffraction patterns of neat PLA and the blends.

Table 6
Apparent crystallite size calculations for PLA/PHI.

Peak position (2θ)	FWHM (β)	Apparent crystallite Size (nm)	Possible crystal plane
13.93	5.92	1.4	(110) or PHA-related
16.70	1.56	5.1	(110)/(200) of PLA α-form
20.11	4.25	1.9	(203) or (015) of PLA
25.34	5.20	1.6	Higher order reflection
26.82	0.28	29.2	Larger crystallite phase
30.80	2.74	3.0	Higher order reflection

Table 7
Apparent crystallite size calculations for PLA/PHAS.

Peak position (2θ)	FWHM (β)	Apparent crystallite Size (nm)	Possible crystal plane
14.57	10.71	0.8	(110) or PHA-related
16.51	1.04	7.7	(110)/(200) of PLA α-form
21.33	5.33	1.5	(203) or (015) of PLA
25.37	0.34	24.3	Larger crystallite phase
26.80	3.06	2.7	Higher order reflection
30.83	8.26	1.0	Higher order reflection

3.7. Flexural properties analysis

Neat PLA exhibits typical semi-brittle behavior, with a relatively low peak stress and an early drop in load-bearing capacity. Both blends show a markedly stronger response, characterized by higher peak stresses and a more extended deformation region before failure. Representative flexural stress–strain curves for neat PLA, PLA/PHAS, and PLA/PHI are shown in Fig. 8.

We indicated the limiting conventional flexural strain (3.5%), under which the specimen can be considered a straight beam, with a dashed line. The figure shows that the stress maxima occurred at strains above this value. To evaluate the entire test, we used nonlinear corrections for calculating the stresses and strains, according to the standard (see 2.4.7).

Neat PLA gives a flexural strength of 54.81 ± 2.97 MPa and a flexural modulus of 1.98 ± 0.10 GPa. The neat PLA has a peak load and shows the initial failure at around 3.60 ± 0.33% strain. Even though PLA/PHAS and PLA/PHI are also rigid plastics, they reach their maximum stress at significantly higher strains. The blending formulation successfully addressed the inherent fragility and moderate load capacity of neat PLA by increasing the flexural toughness. Flexural properties are presented in Table 8.

The PLA/PHAS blend demonstrates enhancements in all flexural properties compared to neat PLA. Its flexural strength increases by approximately 43%, and its flexural strain at peak load is 1.6 times greater. Additionally, its flexural modulus increases by around 18%. Consequently, the PLA/PHAS blend effectively combines reinforcement

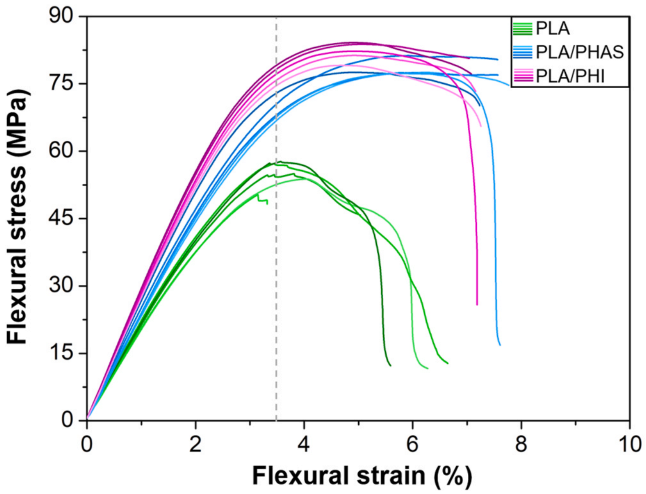

Fig. 8. Flexural stress–strain curves from three-point bending tests (n = 5 per material). Different shades of the same color represent individual test specimens. The vertical dashed line at 3.5% strain indicates the boundary between the small- and large-deformation regimes, where nonlinear geometric corrections were applied.

Table 8
Flexural properties of PLA, PLA/PHAS, and PLA/PHI blends with standard deviations.

Specimens	Flexural strength (MPa)	Flexural strain at maximum flexural stress (%)	Flexural modulus (GPa)	Flexural toughness (MJ/m^3)
PLA	54.81 ± 2.97	3.60 ± 0.33	1.98 ± 0.10	2.00 ± 0.60
PLA/PHAS	78.22 ± 1.71	5.73 ± 0.51	2.33 ± 0.11	4.45 ± 0.13
PLA/PHI	82.14 ± 2.05	4.91 ± 0.13	2.68 ± 0.07	4.49 ± 0.07

with increased toughness. Conversely, the PLA/PHI blend exhibits even more significant modifications. Compared with neat PLA, it shows a 50% increase in flexural strength and a 35% increase in flexural modulus. Despite its high stiffness, its strain at peak load still shows a major improvement, increasing by more than a third compared to neat PLA. The blends' flexural toughness increases by 120–125% compared to neat PLA, indicating a significant enhancement in energy adsorption.

Comparing the two blends, PLA/PHI demonstrates load-bearing capacity. PLA/PHI's maximum flexural strength is 5% higher than that of PLA/PHAS, and its modulus is 15% greater. These variations in flexural behavior suggest that the blends may exhibit different time-dependent deformation under sustained load, as considered in the next section.

3.8. Viscoelastic behavior: experimental observations and model validation

We characterized the viscoelastic response of the PLA/PHA blends using a finite-element model in ANSYS Workbench. A Prony-series representation (generalized Maxwell model) describes time-dependent behavior. We obtained Prony parameters by fitting the experimental creep modulus-versus-time curves using least squares. Four Prony terms offer a practical balance between fitting stability and simulation accuracy.

To exploit test symmetry, we modeled a half-geometry of the three-point bending specimen. We halved the applied force accordingly and solve the problem in 2D under a plane-stress assumption. Fig. 9 shows the resulting finite-element mesh and boundary conditions. The part was meshed with second-order (8-node) quad elements (Plane 183 in ANSYS Workbench). This element type allows excellent solution accuracy for 2D simulations. The FE mesh consisted of 2960 elements and 9217 nodes, providing sufficient density for an accurate solution.

The FE simulations successfully reproduce the expected three-point bending kinematics. Maximum deflection occurs at midspan, with displacement decreasing smoothly toward the supports. Fig. 10 shows a representative deformed shape for a PLA–PHA specimen at 25 °C (displacements scaled ×10 for visibility). The absence of false numerical artifacts confirms that the model correctly captures bending mechanics.

We validated the model by directly comparing simulated and experimental loading nose displacement versus time curves for PLA/PHAS (Fig. 11) and PLA/PHI (Fig. 12). The model accurately predicts the experimental response for small deformations and at temperatures well below T_g. Specifically, accurate predictions hold up to ~40 °C for PLA/PHAS and up to ~45 °C for PLA/PHI. Above these temperatures, however, the measured displacements are noticeably larger than the predictions of the model. At about 45–50 °C, the materials enter their glass transition region. Molecular mobility increases sharply in this range, producing time-dependent, nonlinear deformations. This behavior suggests that the applied load no longer falls within the linear viscoelastic region under these conditions. Near T_g, even moderate stresses (such as 2 MPa) can induce a nonlinear response [66]. As a result, the linear Prony model, parameterized from sub-T_g data, cannot capture this behavior. This discrepancy has a clear physical basis. Below T_g, the polymer behaves as a glass, with highly constrained chain motion and deformation dominated by bond stretching and small-scale relaxations. In this regime, linear viscoelasticity and the generalized Maxwell model provide an accurate description. Near and above T_g, however, cooperative segmental motion becomes significant. Large-scale chain rearrangements occur, leading to nonlinear, temperature-dependent creep and recovery. Because the Prony parameters are derived from sub-T_g data, the model underestimates the amplified displacements observed during and after the transition.

Fig. 13 shows the measured and simulated creep modulus time curves for the PLA/PHAS grade Fig. 14 for the PLA/PHI grade. Curve

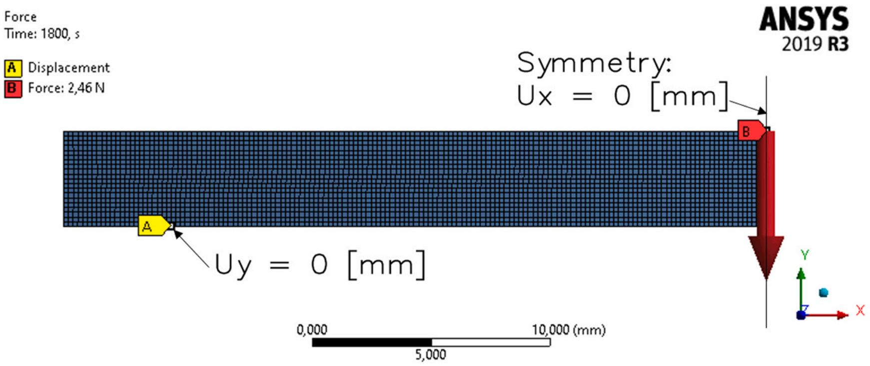

Fig. 9. The FE simulation model.

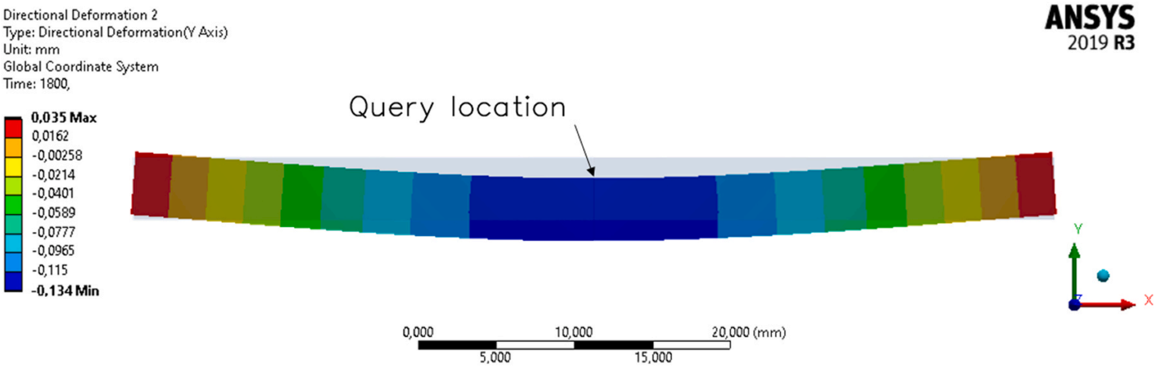

Fig. 10. The vertical (Y-directional) deformation of the PLA-PHA specimen at 25 °C. The deformations are scaled up by a factor of 10.

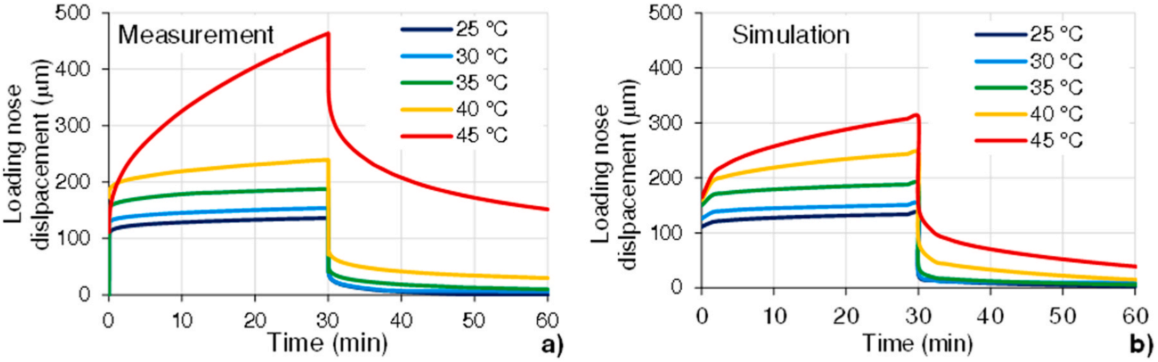

Fig. 11. The comparison of the clamp displacement measured during the testing of the PLA/PHAS specimen at various temperatures.

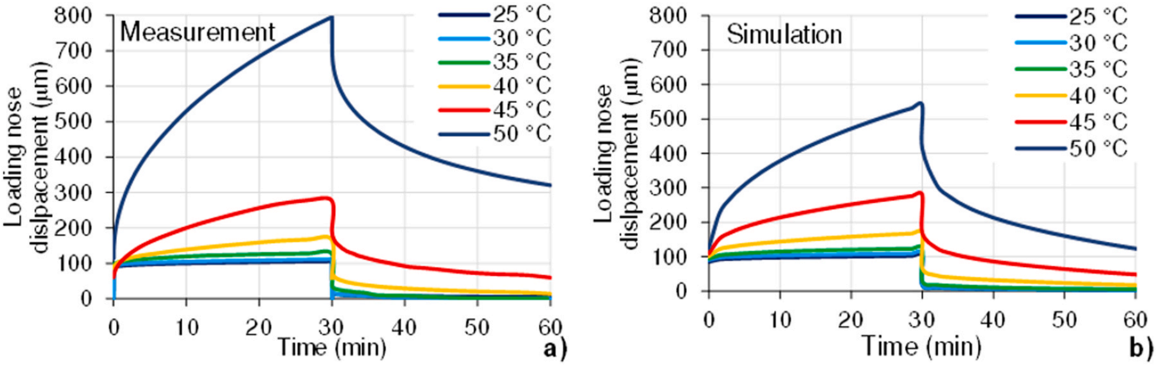

Fig. 12. The comparison of the clamp displacement measured during the testing of the PLA/PHI specimen at various temperatures.

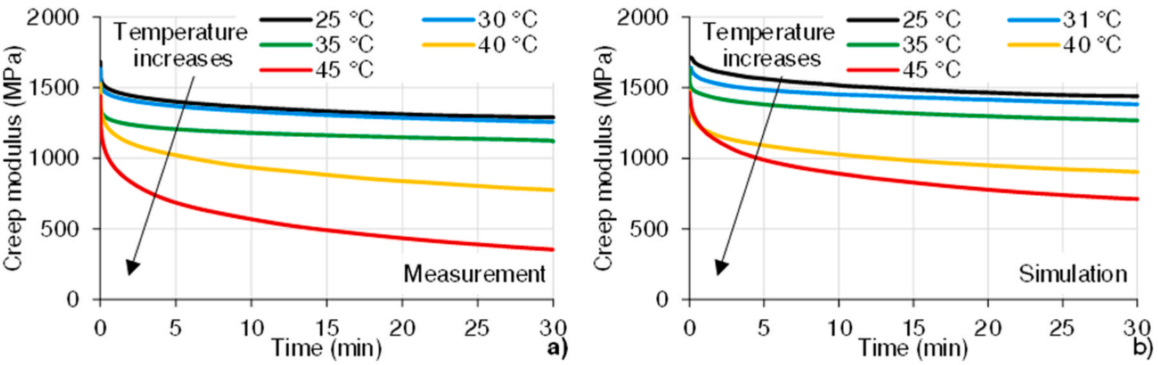

Fig. 13. The measured a) and the simulated b) creep modulus – time curves at various temperatures for the PLA/PHAS specimen.

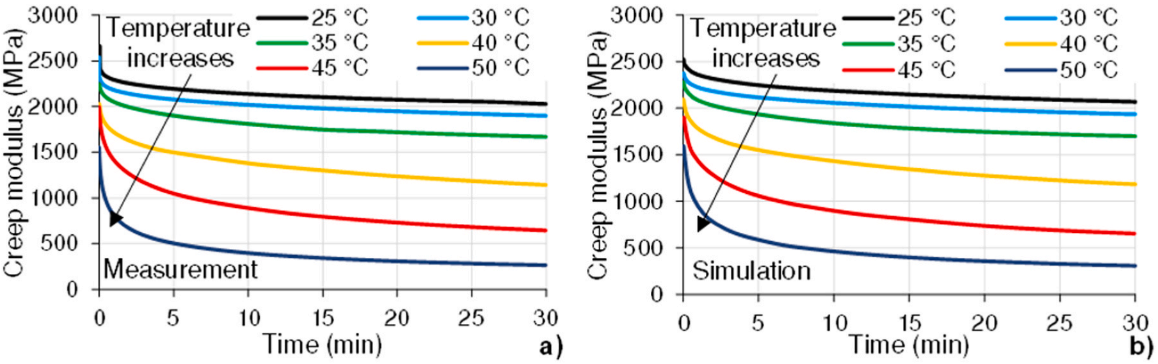

Fig. 14. The measured a) and the simulated b) creep modulus – time curves at various temperatures for the PLA/PHI specimen.

fitting in the FE model was performed with the use of the least squares method, based on the measurements.

The numerical comparison of the measured and the simulated loading nose displacements is shown in Table 9. The displacements were extracted at 25 min because a slight numerical transient occurs at 30 min due to the sudden unloading of the structure. The comparison shows that the modeling method accurately reproduced the measured results.

A Comparison of the two blends reveals an application-relevant difference. PLA/PHI exhibits more accurate, predictable creep behavior at higher temperatures (~45 °C) than PLA/PHAS (~40 °C). This greater dimensional stability at temperatures approaching physiological conditions (37 °C) agrees with the XRD results. The PHI blend exhibits a more developed, coherent crystalline network. Such ordered domains physically constrain amorphous chains and delay the onset of large-scale molecular mobility. Thus, the composition-dependent thermomechanical stability observed in creep tests directly links to the crystalline architecture revealed by XRD.

In summary, FE plus the Prony-series approach reliably models linear viscoelastic bending behavior. It is suitable for predicting dimensional stability under load at temperatures below T_g. To accurately predict behavior through and above T_g, the model requires extension. Potential improvements include integrating nonlinear viscoelasticity with temperature-dependent relaxation spectra and continuously recalibrating the model to improve accuracy. Such approaches become necessary when actuated or recovery cycles are designed that track glass transition.

4. Conclusions

In this study, we demonstrated that blending PLA with semi-crystalline PHAS or PHI (30 wt%) yielded FFF 3D-printable filaments with distinct morphological, thermal, and viscoelastic properties. Both blends exhibited higher melt elasticity and greater temperature sensitivity than neat PLA. PLA/PHAS showed the lowest viscosity at 220 °C and the strongest temperature-dependent viscosity change. SEM and AFM confirmed a heterogeneous two-phase morphology in both blends. PLA/PHAS exhibited finer and more uniformly dispersed PHA domains than PLA/PHI.DSC revealed two glass transitions and reduced PLA cold crystallization, confirming immiscibility in PLA and restricted chain mobility.

XRD analysis showed that neat PLA printed under identical conditions formed only mesomorphic domains (crystallite size ~0.8 nm). In contrast, PLA/PHAS and PLA/PHI developed hierarchical crystalline structures containing large crystallites of 24.3 nm and 29.2 nm, respectively, alongside smaller crystallites averaging ~6–7 nm. As with all estimates based on Scherrer's method, these values should be regarded as semi-quantitative (apparent crystallite sizes). This is because the Scherrer equation estimates domain sizes from peak broadening, which may arise from multiple microstructural factors beyond crystallite size alone. Consequently, we presented these values as relative markers of structural trends rather than absolute measurements. The degree of crystallinity from XRD was 16.0% for PLA/PHAS and 19.3% for PLA/PHI. These well-ordered crystallites served as structural domains that contributed to stiffness and dimensional stability. Flexural characterization confirmed these structural improvements, showing that both blend formulations successfully addressed the limited flexibility and moderate strength of the neat PLA. Notably, while neat PLA failed at the start of the large-deformation stage, both blends extended beyond the 3.5% strain limit without cracking, reaching their maximum load capacity deep in the non-linear region. The resulting mechanical profiles revealed a clear trade-off: the PLA/PHI system provided enhanced rigidity and structural stiffness, while the PLA/PHAS blend maintained a significant advantage in peak flexibility. The Prony-series finite element model accurately predicted linear viscoelastic behavior below the glass-transition region. The model remained reliable up to approximately 40 °C for PLA/PHAS and 45 °C for PLA/PHI.

Overall, the results demonstrate that the incorporation of PHA enables control of crystalline structure and viscoelastic response in PLA-based materials. Based on their morphology, thermal properties, and hierarchical crystallinity, the blends are promising candidates for a further study of thermomechanical behavior. However, direct experimental validation—specifically, the measurement of shape fixity and recovery ratios through thermomechanical cycling—is necessary to confirm this perspective. Future research will examine various PLA/PHA blend ratios to establish clear quantitative relationships between composition, structure, and properties. Future work will also include thermomechanical cycling and direct evaluation of shape recovery and fixity. Furthermore, integrating nanofiber mats into the blend will be investigated as a strategy to further enhance mechanical performance and thermal response.

Table 9
Comparison of the measured and the simulated loading nose displacements.

Temperature (°C)	Measured displacement (μm)		Simulated displacement (μm)		Relative error in the percentage of measurement (%)	
	PLA/PHAS	PLA/PHI	PLA/PHAS	PLA/PHI	PLA/PHAS	PLA/PHI
25	133	105	133	101	−0.3	3.8
30	153	110	150	108	2.0	1.8
35	186	127	187	122	−0.6	3.9
40	237	165	241	164	−1.5	0.6
45	445	275	301	268	32.4	2.5

CRediT authorship contribution statement

Kardo Khalid Abdullah: Writing – review & editing, Writing – original draft, Visualization, Validation, Software, Resources, Project administration, Methodology, Investigation, Formal analysis, Data curation, Conceptualization. **Szabolcs Krizsma:** Writing – review & editing, Validation, Software, Formal analysis, Data curation. **Péter Széplaki:** Writing – review & editing, Data curation. **Kolos Molnár:** Writing – review & editing, Supervision, Project administration, Funding acquisition, Conceptualization.

Declaration of Competing Interest

The authors declare that they have no known competing financial interests or personal relationships that could have appeared to influence the work reported in this paper.

Acknowledgments

This research was funded by the National Research, Development and Innovation Office (STARTING 153178). The authors acknowledge the Ministry of Culture and Innovation of Hungary for support from the National Research, Development and Innovation Fund through grant no. NKKP STARTING 152873. Project no. KDP-IKT−2023–900-I1–00000957/0000003 has been implemented with the support provided by the Ministry of Culture and Innovation of Hungary from the National Research, Development and Innovation Fund, financed under the KDP−2023 funding scheme. Kolos Molnár is thankful for the support of the János Bolyai Research Scholarship of the Hungarian Academy of Sciences.

Appendix A. Supporting information

Supplementary data associated with this article can be found in the online version at doi:10.1016/j.mtcomm.2026.115546.

Data availability

Data will be made available on request.

References

[1] A. Babakhani, S.J. Peighambardoust, M. Ghahremani-Nasab, N. S. Peighambardoust, Fabrication of biodegradable nanocomposite scaffolds with hydroxyapatite, magnetic clay, and graphene oxide for bone tissue engineering, Sci. Rep. 15 (1) (2025) 22235, https://doi.org/10.1038/s41598-025-07270-5.

[2] K.K. Abdullah, K. Molnár, Current trends and future prospects of integrating electrospinning with 3D printing techniques for mimicking bone extracellular matrix scaffolds, J. Polym. Sci. 63 (6) (2025) 1481–1504, https://doi.org/10.1002/pol.20241010.

[3] J. Żur-Pińska, M.Z. Gładysz, D. Ubels, J. Siebring, M.K. Włodarczyk-Biegun, Smart and sustainable: exploring the future of PHAs biopolymers for 3D printing in tissue engineering, Sustain. Mater. Technol. 38 (2023) e00750, https://doi.org/10.1016/j.susmat.2023.e00750.

[4] M. Ďurfina, N. Babaei, Z. Vanovčanová, J. Feranc, V. Horváth, I. Vašková, J. Kruželák, K. Tomanová, R. Plavec, Bio-based polyhydroxyalkanoate (PHA) blends for 3D printing: rheological, mechanical, biocompatibility, and biodegradation properties, Polymers 17 (11) (2025) 1477, https://doi.org/10.3390/polym17111477.

[5] T. Pulingam, J.N. Appaturi, T. Parumasivam, A. Ahmad, K. Sudesh, Biomedical applications of polyhydroxyalkanoate in tissue engineering, Polymers 14 (11) (2022) 2141, https://doi.org/10.3390/polym14112141.

[6] StefaniakMasek, Poly(lactic acid) (PLA) – short review of synthesis methods, properties, recent progress, and new challenges, Express Polym. Lett. 19 (2025) 386–408, https://doi.org/10.3144/expresspolymlett.2025.29.

[7] A. Ding, F. Tang, E. Alsberg, The emerging 4D printing of shape-memory thermomorphs for self-adaptative biomedical implants, Adv. Funct. Mater. 35 (28) (2025) 2418348, https://doi.org/10.1002/adfm.202418348.

[8] S. Başkır, A.O. Cankaya, E. Tekay, B. Erenay, B. Garipcan, Ö. Kocatürk, Shape memory polyurethane synthesis using glycerol as chain extender for biomedical applications, Polym. Int. 74 (4) (2025) 336–345, https://doi.org/10.1002/pi.6725.

[9] J. Ji, K. Zhang, X. Guo, Shape memory polymer lattice structures with programmable thermal recovery time, Smart Mater. Struct. 33 (8) (2024) 085027, https://doi.org/10.1088/1361-665X/ad6227.

[10] B. Tatár, L. Mészáros, Shape memory characteristics of injection molded poly(lactic acid) multiscale hybrid composites, ACS Omega 9 (47) (2024) 46960–46967, https://doi.org/10.1021/acsomega.4c06592.

[11] K.Y. Shen, X.J. Wang, H.J. Chen, Advances in light-activated shape memory polymer: A brief review, Mater. Today Commun. 41 (2024) 110247, https://doi.org/10.1016/j.mtcomm.2024.110247.

[12] M.R. Pfau, K.G. McKinzey, A.A. Roth, L.M. Graul, D.J. Maitland, M.A. Grunlan, Shape memory polymer (SMP) scaffolds with improved self-fitting properties, J. Mater. Chem. B 9 (18) (2021) 3826–3837, https://doi.org/10.1039/D0TB02987D.

[13] P.A. Zhukova, F.S. Senatov, M.Y. Zadorozhnyy, N.S. Chmelyuk, V.A. Zaharova, Polymer composite materials based on polylactide with a shape memory effect for “self-fitting” bone implants, Polymers 13 (14) (2021) 2367, https://doi.org/10.3390/polym13142367.

[14] S.B. Gasson, L.K. Dobson, M.R. Pfau-Cloud, F.O. Beltran, R.R. Pool, C.A. Gregory, M.A. Grunlan, W.B. Saunders, Biocompatibility and bone regeneration by shape memory polymer scaffolds, J. Biomed. Mater. Res. Part. A 113 (1) (2025) e37806, https://doi.org/10.1002/jbm.a.37806.

[15] L. Cao, L. Wang, C. Zhou, X. Hu, L. Fang, Y. Ni, C. Lu, Z. Xu, Surface structures, particles, and fibers of shape-memory polymers at micro-/nanoscale, Adv. Polym. Technol. 2020 (1) (2020) 7639724, https://doi.org/10.1155/2020/7639724.

[16] J. Hu, Y. Zhu, H. Huang, J. Lu, Recent advances in shape–memory polymers: Structure, mechanism, functionality, modeling and applications, Prog. Polym. Sci. 37 (12) (2012) 1720–1763, https://doi.org/10.1016/j.progpolymsci.2012.06.001.

[17] T. Dayyoub, A.V. Maksimkin, O.V. Filippova, V.V. Tcherdyntsev, D.V. Telyshev, Shape memory polymers as smart materials: a review, Polymers 14 (17) (2022) 3511, https://doi.org/10.3390/polym14173511.

[18] K. Litauszki, R. Petrény, Z. Haramia, L. Mészáros, Combined effects of plasticizers and D-lactide content on the mechanical and morphological behavior of polylactic acid, Heliyon 9 (4) (2023), https://doi.org/10.1016/j.heliyon.2023.e14674.

[19] L.P. Nori, S. Manikiran, An outlook on regulatory aspects of 3D printing in pharmaceutical and medical sectors, Curr. Trends Pharm. Pharm. Chem. 4 (3) (2022) 98–108, https://doi.org/10.18231/j.ctppc.2022.017.

[20] G. Narayanan, V.N. Vernekar, E.L. Kuyinu, C.T. Laurencin, Poly (lactic acid)-based biomaterials for orthopaedic regenerative engineering, Adv. Drug. Deliv. Rev. 107 (2016) 247–276, https://doi.org/10.1016/j.addr.2016.04.015.

[21] S. Farah, D.G. Anderson, R. Langer, Physical and mechanical properties of PLA, and their functions in widespread applications — a comprehensive review, Adv. Drug. Deliv. Rev. 107 (2016) 367–392, https://doi.org/10.1016/j.addr.2016.06.012.

[22] J. Sringam, T. Kajornprai, T. Trongsatitkul, N. Suppakarn, Shape memory performance and microstructural evolution in PLA/PEG blends: role of plasticizer content and molecular weight, Polymers 17 (2) (2025) 225, https://doi.org/10.3390/polym17020225.

[23] A. Ghaznavi Youvalari, J. Alizadeh Kaklar, M. Mohamadi, Investigation of mechanical properties in PLA, ABS and epoxy resin parts fabricated by 3D printing technology, Sci. Rep. 15 (1) (2025) 27777, https://doi.org/10.1038/s41598-025-13866-8.

[24] Z. Ye, P. Hou, L. Zhang, Preparation and characterization of PLA/TPU/HA enhanced shape memory blends, Mater. Today Commun. 47 (2025) 113023, https://doi.org/10.1016/j.mtcomm.2025.113023.

[25] K.K. Abdullah, K. Molnár, Enhancing crystallinity of electrospun polylactic acid fibers: insights into formation mechanisms and property modulation–a review, Macromol. Mater. Eng. 311 (2026) e00368, https://doi.org/10.1002/mame.202500368.

[26] S.K. Leist, D. Gao, R. Chiou, J. Zhou, Investigating the shape memory properties of 4D printed polylactic acid (PLA) and the concept of 4D printing onto nylon fabrics for the creation of smart textiles, Virtual Phys. Prototyp. 12 (4) (2017) 290–300, https://doi.org/10.1080/17452759.2017.1341815.

[27] Z. Liu, Y. Li, S. Ma, C. Liu, Y. Zhang, X. Lu, Z. Lin, Y. Liang, Near-infrared light-driven programmable shape memory polymer for self-shaping 3D printing methods, Virtual Phys. Prototyp. 19 (1) (2024) e2422384, https://doi.org/10.1080/17452759.2024.2422384.

[28] D. Nie, X. Yin, Z. Cai, J. Wang, Effect of crystallization on shape memory effect of poly(lactic acid), Polymers 14 (8) (2022) 1569, https://doi.org/10.3390/polym14081569.

[29] B. Cecen, FDM-based 3D printing of PLA/PHA composite polymers, Chem. Pap. 77 (8) (2023) 4379–4386, https://doi.org/10.1007/s11696-023-02786-4.

[30] S. Cai, Y.-C. Sun, J. Ren, H.E. Naguib, Toward the low actuation temperature of flexible shape memory polymer composites with room temperature deformability via induced plasticizing effect, J. Mater. Chem. B 5 (44) (2017) 8845–8853, https://doi.org/10.1039/C7TB02068F.

[31] K.K. Abdullah, A. Bulátkó, K. Molnár, 3D electrospinning of highly porous, custom-shaped nanofiber structures by a novel method, Results Eng. 29 (2026) 108740, https://doi.org/10.1016/j.rineng.2025.108740.

[32] M. Koller, D. Heeney, A. Mukherjee, Biodegradability of polyhydroxyalkanoate (PHA) biopolyesters in nature: a review, Biodegradation 36 (4) (2025) 76, https://doi.org/10.1007/s10532-025-10164-y.

[33] D. Li, Y. Yang, R. Liu, Y. Wu, F. Guo, Review of biopolymer polyhydroxybutyrate (PHB) and blends: modification of thermal and mechanical properties via additive manufacturing processing, Polymers 17 (22) (2025) 3083, https://doi.org/10.3390/polym17223083.

[34] W. Kanabenja, N. Passornraprasit, C. Aumnate, T.A. Osswald, D. Aht-Ong, P. Potiyaraj, Enhancing 3D printability of polyhydroxybutyrate (PHB) and poly(3-hydroxybutyrate-co-3-hydroxy valerate) (PHBV) based blends through melt extrusion based-3D printing, Addit. Manuf. 86 (2024) 104205, https://doi.org/10.1016/j.addma.2024.104205.

[35] A. Apicella, P. Scarfato, L. Incarnato, Study on 3D printability of PLA/PBAT/PHBV biodegradable blends for packaging applications, Polym. Test. 145 (2025) 108748, https://doi.org/10.1016/j.polymertesting.2025.108748.

[36] I. Burzic, C. Pretschuh, D. Kaineder, G. Eder, J. Smilek, J. Másilko, W. Kateryna, Impact modification of PLA using biobased biodegradable PHA biopolymers, Eur. Polym. J. 114 (2019) 32–38, https://doi.org/10.1016/j.eurpolymj.2019.01.060.

[37] Pouriman, Graham, Jayaraman, Monolayer films from poly(lactic acid) PLA/poly (3-hydroxybutyrate-co-hydroxyvalerate) PHBV blends for food packaging applications, Express Polym. Lett. 17 (2023) 1007–1018, https://doi.org/10.3144/expresspolymlett.2023.75.

[38] K. Olonisakin, A.K. Mohanty, M. Thimmanagari, M. Misra, Recent advances in biodegradable polymer blends and their biocomposites: a comprehensive review, Green. Chem. 27 (38) (2025) 11656–11704, https://doi.org/10.1039/D5GC01294E.

[39] T. Gerard, T. Budtova, A. Podshivalov, S. Bronnikov, Polylactide/poly (hydroxybutyrate-co-hydroxyvalerate) blends: Morphology and mechanical properties, Express Polym. Lett. 8 (2014) 609–617, https://doi.org/10.3144/expresspolymlett.2014.64.

[40] D. Rahmatabadi, M. Khajepour, A. Bayati, K. Mirasadi, M. Amin Yousefi, A. Shegeft, I. Ghasemi, M. Baniassadi, K. Abrinia, M. Bodaghi, M. Baghani, Advancing sustainable shape memory polymers through 4D printing of polylactic acid-polybutylene adipate terephthalate blends, Eur. Polym. J. 216 (2024) 113289, https://doi.org/10.1016/j.eurpolymj.2024.113289.

[41] A. Sabalina, S. Gaidukovs, A. Aunins, A. Gromova, G. Gaidukova, L. Orlova, O. Platnieks, Exploring the processing potential of polylactic acid, polyhydroxyalkanoate, and poly(butylene succinate-co-adipate) binary and ternary blends, Polymers 16 (16) (2024) 2288, https://doi.org/10.3390/polym16162288.

[42] I. Vozniak, R. Hosseinnezhad, J. Morawiec, A. Galeski, Nanofibrillar green composites of polylactide/polyhydroxyalkanoate produced in situ due to shear induced crystallization, Polymers 11 (11) (2019) 1811, https://doi.org/10.3390/polym11111811.

[43] I. Jalan, L.K.E. Ericsson, E. Moons, J. van Stam, AFM-IR spectromicroscopy unveils hidden phase separation in polymer–polymer blend films for photovoltaic applications, ACS Appl. Polym. Mater. 6 (18) (2024) 11312–11319, https://doi.org/10.1021/acsapm.4c01883.

[44] S. Kuwashiro, K. Tao, H. Kishi, M. Nakamura, Phase-separated structure and optical properties of simultaneously polymerized polymethacrylate/polyurethane blends, Polym. J. 58 (3) (2026) 235–243, https://doi.org/10.1038/s41428-025-01120-x.

[45] T. Ohshida, T. Wada, T. Kaneuchi, E. Ohno, T. Taniike, Data-driven phase analysis of immiscible polymer blends via multi-parameter AFM imaging, Polymer 343 (2026) 129391, https://doi.org/10.1016/j.polymer.2025.129391.

[46] K. Takamatsu, H. Saito, AFM observation of crystalline morphologies developed by cooperative progress with spinodal decomposition in dissimilar polycarbonate blends, Polym. J. 54 (6) (2022) 815–820, https://doi.org/10.1038/s41428-022-00624-0.

[47] N. Prine, Z. Cao, S. Zhang, T. Li, C. Do, K. Hong, C. Cardinal, T.L. Thornell, S. E. Morgan, X. Gu, Enabling quantitative analysis of complex polymer blends by infrared nanospectroscopy and isotopic deuteration, Nanoscale 15 (16) (2023) 7365–7373, https://doi.org/10.1039/D3NR00886J.

[48] M. Cvetkoski, H. Najaf Zadeh, Exploring commercial PHA filament for more eco-friendly 3D printing, Manuf. Lett. 47 (2026) 32–37, https://doi.org/10.1016/j.mfglet.2025.12.005.

[49] J. Gonzalez Ausejo, J. Rydz, M. Musioł, W. Sikorska, M. Sobota, J. Włodarczyk, G. Adamus, H. Janeczek, I. Kwiecień, A. Hercog, B. Johnston, H.R. Khan, V. Kannappan, K.R. Jones, M.R. Morris, G. Jiang, I. Radecka, M. Kowalczuk, A comparative study of three-dimensional printing directions: the degradation and toxicological profile of a PLA/PHA blend, Polym. Degrad. Stab. 152 (2018) 191–207, https://doi.org/10.1016/j.polymdegradstab.2018.04.024.

[50] N. Vidakis, M. Petousis, N. Mountakis, M. Spyridaki, K. Gkagkanatsiou, E. Stratakis, Optimization of main process control parameters of PHA bio-polymer in material extrusion additive manufacturing: experimental design and predictive models, Int. J. Adv. Manuf. Technol. 139 (3) (2025) 1607–1623, https://doi.org/10.1007/s00170-025-15978-x.

[51] M. Petousis, N. Michailidis, N. Mountakis, A. Argyros, M. Spyridaki, E. Maravelakis, N. Nasikas, N. Vidakis, The impact of MEX 3D printing key control settings on the rheology and DMA response of bacteria-derived PHA, ACS Omega 10 (25) (2025) 27632–27647, https://doi.org/10.1021/acsomega.5c04386.

[52] C. Huang, S.-L. Zheng, M. Lee, Preliminary insights into the photosensitivity of bio-based plastics: release of microplastic-derived organic matter in water under UV irradiation, Environ. Pollut. 367 (2025) 125619, https://doi.org/10.1016/j.envpol.2024.125619.

[53] N. Vidakis, C. David, D. Sagris, K. Gkagkanatsiou, I. Valsamos, A. Moutsopoulou, N. K. Nasikas, M. Petousis, Critical quality indicators assessment in MEX additive manufacturing with bacteria-derived PHA: the effect of process control parameters, Int. J. Adv. Manuf. Technol. 140 (7) (2025) 4213–4233, https://doi.org/10.1007/s00170-025-16518-3.

[54] B.L. Seregi, P. Ficzere, Development of part cooling in 3D printer through the design of a custom cooling duct using generative design, Period. Polytech. Mech. Eng. 69 (4) (2025) 392–396, https://doi.org/10.3311/PPme.42624.

[55] W.J. Hendrikson, C.A. van Blitterswijk, J. Rouwkema, L. Moroni, The use of finite element analyses to design and fabricate three-dimensional scaffolds for skeletal tissue engineering, Front. Bioeng. Biotechnol. 5 (2017) 1–13, https://doi.org/10.3389/fbioe.2017.00030.

[56] R. Luo, H. Lv, H. Liu, Development of Prony series models based on continuous relaxation spectrums for relaxation moduli determined using creep tests, Constr. Build. Mater. 168 (2018) 758–770, https://doi.org/10.1016/j.conbuildmat.2018.02.036.

[57] A. Jayswal, J. Liu, G. Harris, R. Mailen, S. Adanur, Creep behavior of 3D printed polymer composites, Polym. Eng. & Sci. 63 (11) (2023) 3809–3818, https://doi.org/10.1002/pen.26486.

[58] W. Crupano, B. Adrover-Monserrat, J. Llumà, D. Sánchez-Molina, R. Jerez-Mesa, J. A. Travieso-Rodriguez, Analysis of the viscoelastic properties of 3D-printed PLA/PHB, Progress. Addit. Manuf. (2026), https://doi.org/10.1007/s40964-025-01474-x.

[59] A. Aniskevich, R. Joffe, S. Tarasovs, O. Bulderberga, S. Stankevich, J. Sevcenko, O. Volodins, Methodology for predicting the long-term deformability of 3D-printed polymer structures, Mech. Compos. Mater. 61 (6) (2026) 1143–1168, https://doi.org/10.1007/s11029-026-10331-z.

[60] B. Liu, Y. Pan, Effect of pore shape on mechanical properties of porous shape memory alloy, Micromachines 13 (4) (2022) 566, https://doi.org/10.3390/mi13040566.

[61] C. Witherspoon, P. Zheng, M. Chmielus, D.C. Dunand, P. Müllner, Effect of porosity on the magneto-mechanical behavior of polycrystalline magnetic shape-memory Ni–Mn–Ga foams, Acta Mater. 92 (2015) 64–71, https://doi.org/10.1016/j.actamat.2015.03.038.

[62] E. Fischer, H.J. Sterzel, G. Wegner, Investigation of the structure of solution grown crystals of lactide copolymers by means of chemical reactions, Kolloid-Zeitschrift Zeitschrift für Polym. 251 (1973) 980–990, https://doi.org/10.1007/BF01498927.

[63] P.J. Barham, A. Keller, E.L. Otun, P.A. Holmes, Crystallization and morphology of a bacterial thermoplastic: poly-3-hydroxybutyrate, J. Mater. Sci. 19 (9) (1984) 2781–2794, https://doi.org/10.1007/BF01026954.

[64] P. Scherrer, Nachrichten von der Gesellschaft der Wissenschaften zu Göttingen, Mathematisch-Physikalische Klasse 2 (1918) 98-100.

[65] ASTM International, ASTM D790-10, Standard Test Methods for Flexural Properties of Unreinforced and Reinforced Plastics and Electrical Insulating Materials, ASTM International, West Conshohocken, PA, 2010, https://doi.org/10.1520/D0790-10.

[66] R.G. Ricarte, S. Shanbhag, A tutorial review of linear rheology for polymer chemists: basics and best practices for covalent adaptable networks, Polym. Chem. 15 (9) (2024) 815–846, https://doi.org/10.1039/d3py01367g.

[67] A. Shabbir, H. Goldansaz, O. Hassager, E. van Ruymbeke, N.J. Alvarez, Effect of hydrogen bonding on linear and nonlinear rheology of entangled polymer melts, Macromolecules 48 (16) (2015) 5988–5996, https://doi.org/10.1021/acs.macromol.5b00757.

[68] R. Arrigo, A. Frache, FDM printability of PLA based-materials: the key role of the rheological behavior, Polymers 14 (9) (2022) 1754, https://doi.org/10.3390/polym14091754.

[69] G. Bernagozzi, D. Battegazzore, R. Arrigo, A. Frache, Optimizing the rheological and thermal behavior of polypropylene-based composites for material extrusion additive manufacturing Processes, Polymers 15 (10) (2023) 2263, https://doi.org/10.3390/polym15102263.

[70] H. Torabi, H. McGreal, H. Zarrin, E. Behzadfar, Effects of rheological properties on 3D printing of poly(lactic acid) (PLA) and poly(hydroxy alkenoate) (PHA) hybrid materials, ACS Appl. Polym. Mater. 5 (6) (2023) 4034–4044, https://doi.org/10.1021/acsapm.3c00271.

[71] L. Li, W. Huang, B. Wang, W. Wei, Q. Gu, P. Chen, Properties and structure of polylactide/poly (3-hydroxybutyrate-co-3-hydroxyvalerate) (PLA/PHBV) blend fibers, Polymer 68 (2015) 183–194, https://doi.org/10.1016/j.polymer.2015.05.024.

[72] S. Koido, T. Kawai, S. Kuroda, K. Nishida, T. Kanaya, M. Kato, T. Kurose, K. Nakajima, Mesomorphic phase formation of plasticized poly(l-lactic acid), J. Appl. Polym. Sci. 131 (2) (2014), https://doi.org/10.1002/app.39762.

[73] J. Madhavi, Comparison of average crystallite size by X-ray peak broadening and Williamson–Hall and size–strain plots for VO^{2+} doped ZnS/CdS composite nanopowder, SN Appl. Sci. 1 (11) (2019) 1509, https://doi.org/10.1007/s42452-019-1291-9.

[74] A. Fulati, K. Uto, M. Ebara, Influences of crystallinity and crosslinking density on the shape recovery force in poly(ε-caprolactone)-based shape-memory polymer blends, Polymers 14 (21) (2022) 4740, https://doi.org/10.3390/polym14214740.

[75] M. Behl, A. Lendlein, Shape-memory polymers, Mater. Today 10 (4) (2007) 20–28, https://doi.org/10.1016/S1369-7021(07)70047-0.